

A fast ceramic mixed OH⁻/H⁺ ionic conductor for low temperature fuel cells

Received: 8 September 2022

Accepted: 12 January 2024

Published online: 30 January 2024



Peimiao Zou¹, Dinu Iuga², Sanliang Ling³, Alex J. Brown¹, Shigang Chen¹, Mengfei Zhang¹, Yisong Han², A. Dominic Fortes⁴, Christopher M. Howard⁴ & Shanwen Tao^{1,5} ✉

Low temperature ionic conducting materials such as OH⁻ and H⁺ ionic conductors are important electrolytes for electrochemical devices. Here we show the discovery of mixed OH⁻/H⁺ conduction in ceramic materials. SrZr_{0.8}Y_{0.2}O_{3-δ} exhibits a high ionic conductivity of approximately 0.01 S cm⁻¹ at 90 °C in both water and wet air, which has been demonstrated by direct ammonia fuel cells. Neutron diffraction confirms the presence of OD bonds in the lattice of deuterated SrZr_{0.8}Y_{0.2}O_{3-δ}. The OH⁻ ionic conduction of CaZr_{0.8}Y_{0.2}O_{3-δ} in water was demonstrated by electrolysis of both H₂¹⁸O and D₂O. The ionic conductivity of CaZr_{0.8}Y_{0.2}O_{3-δ} in 6 M KOH solution is around 0.1 S cm⁻¹ at 90 °C, 100 times higher than that in pure water, indicating increased OH⁻ ionic conductivity with a higher concentration of feed OH⁻ ions. Density functional theory calculations suggest the diffusion of OH⁻ ions relies on oxygen vacancies and temporarily formed hydrogen bonds. This opens a window to discovering new ceramic ionic conducting materials for near ambient temperature fuel cells, electrolyzers and other electrochemical devices.

Fuel cells are important electrochemical devices to convert chemical energy in fuels into electricity at high efficiency. There are different types of fuel cells based on various ionic conducting electrolytes, with a wide operating temperature from near ambient temperature (≤100 °C) (NAT) e.g., around 80 °C for proton exchange membrane fuel cells (PEMFCs), to high temperature such as 500–900 °C for solid oxide fuel cells (SOFCs)^{1,2}. SOFCs have been developed for stationary power generation while poor durability, due to materials sublimation and cross-diffusion at high operating temperatures, is the major obstacle for the large-scale applications³. The typical electrolyte materials for SOFCs are doped ZrO₂ or CeO₂ with fluorite structures or doped BaCeO₃ (BCO)/BaZrO₃ (BZO)/LaGaO₃ (LGO) with perovskite structures^{1,4–12}. The representative high temperature proton conductors based on doped perovskite oxides BCO/BZO were discovered in 1980 and 1990s respectively^{4,8}, while the high temperature O²⁻ ion conductor based on doped LGO was discovered in 1994^{5,13}. However,

the ionic conductivity of these oxides is not high enough for use in applications when the operating temperature is below 500 °C¹. The minimum required ionic conductivity is approximately 0.01 S cm⁻¹ for use as electrolytes for fuel cells or electrolyzers when thin film technology is applied¹. To solve these problems, it is highly desirable to reduce the operating temperature of SOFCs, ideally to NAT. The first task to achieve NAT operation of SOFCs is to identify good H⁺ / O²⁻ / OH⁻ ionic conducting materials to be used as the electrolyte.

It has been reported that doped zirconates such as BaZr_{0.8}Y_{0.2}O_{3-δ} (BZY020) are robust proton conductors with ionic conductivity above 10⁻⁴ S cm⁻¹ at a temperature above 600 °C^{8,14,15}. In high temperature proton conductors, BZY020 exhibits excellent chemical stability in the presence of steam and CO₂^{9,16}. However, the proton conductivity of perovskite zirconates are normally measured in wet air or wet H₂ by passing the gases through room temperature water with moisture contents of 3 mol%¹⁴. The steam partial pressure may not be high enough to

¹School of Engineering, University of Warwick, Coventry CV4 7AL, UK. ²Department of Physics, University of Warwick, Coventry CV4 7AL, UK. ³Advanced Materials Research Group, Faculty of Engineering, University of Nottingham, Nottingham NG7 2RD, UK. ⁴ISIS Neutron and Muon Spallation Source, Rutherford Appleton Laboratory, Harwell Science and Innovation Campus, Chilton, Oxfordshire OX11 0QX, UK. ⁵Department of Chemical Engineering, Monash University, Clayton, Victoria 3800, Australia. ✉e-mail: S.Tao.1@warwick.ac.uk

achieve the highest possible ionic conductivity. On the other hand, the OH^- ionic conductivity of polymeric alkaline membranes is measured in water¹⁷. For oxide ionic conductors, a high open circuit voltage (OCV) has been reported for electrochemical cells using either 8 mol% Y_2O_3 stabilised ZrO_2 or $\text{Ce}_{0.8}\text{Sm}_{0.2}\text{O}_{2-\delta}$ as the electrolyte while one side is submerged in water, although the real mechanism for this high OCV is still unclear¹⁸. To the best of our knowledge, reports measuring the ionic conductivity of oxides in liquid water are scarce. In this work, we find that for Y-doped AZrO_3 (A = Ca, Sr, Ba), $\text{SrZr}_{0.8}\text{Y}_{0.2}\text{O}_{3-\delta}$ (SZYO20) exhibits the highest ionic conductivity of approximately 0.01 S cm^{-1} at 90°C when exposed in water or humidified air, which opens the window to develop low temperature ceramic OH^- ionic conductors and makes it possible to develop solid oxide fuel cells with an ambient operating temperature, i.e., NAT-SOFCs. Some of the main problems of conventional SOFCs with operating temperatures above 500°C , such as materials sublimation and cross-diffusion, should be alleviated due to the significantly reduced temperatures of NAT operation.

Results

Creation of pathways for ions in perovskite oxide $\text{SrZr}_{1-x}\text{Y}_x\text{O}_{3-\delta}$

For a good ionic conductor, it is necessary to have possible pathways for the diffusion of ions. With the existence of pathways, the concentration of charge carriers must be sufficient in order to achieve high ionic conductivity. For doped zirconates, it is widely accepted that the oxygen vacancies and the associated proton defects during the reaction between oxygen vacancies and steam (or water) form the pathways for the proton conduction^{19,20}. A schematic diagram showing the formation of pathways in a perovskite oxide is shown in Fig. 1. Perovskite oxide SrZrO_3 (SZO) was chosen as the parent phase. When part of Zr at the B-site in SZO is replaced by Y, for charge compensation, positively charged oxygen vacancies ($V_{\text{O}}^{\bullet\bullet}$) are formed. For charge balance, the negatively charged Y'_{Zr} defects are formed simultaneously. It can be described by Kröger-Vink notations.

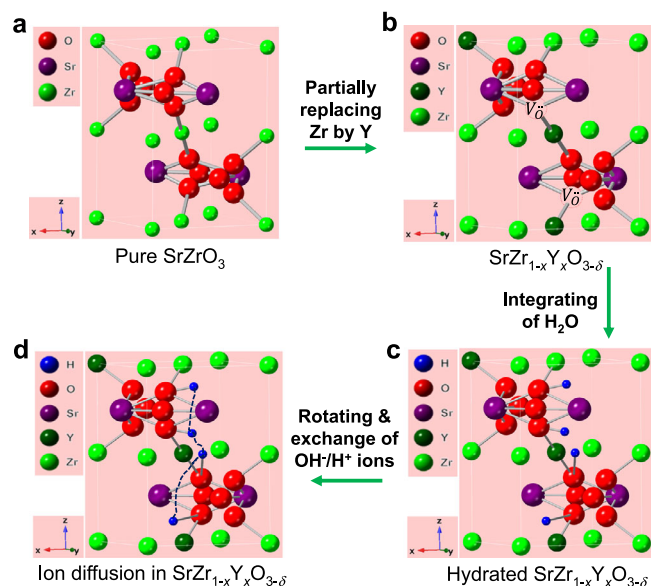
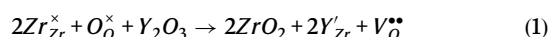
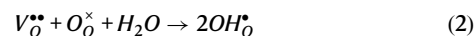


Fig. 1 | The proposed schematic diagram for the formation of pathways for OH^-/H^+ ions in $\text{SrZr}_{1-x}\text{Y}_x\text{O}_{3-\delta}$ enabled by water/steam. a The structure of SrZrO_3 parent phase. **b** The schematic structure of Y doped SrZrO_3 . Part of Zr at the B-site in a is replaced by Y then oxygen vacancies ($V_{\text{O}}^{\bullet\bullet}$) are formed. **c** The schematic structure of hydrated $\text{SrZr}_{1-x}\text{Y}_x\text{O}_{3-\delta}$. Proton defects OH^- are formed in $\text{SrZr}_{1-x}\text{Y}_x\text{O}_{3-\delta}$ after integrating of water or steam. **d** The schematic diagram for OH^-/H^+ ions diffusion in $\text{SrZr}_{1-x}\text{Y}_x\text{O}_{3-\delta}$.

When this Y doped SZO, with a general formula of $\text{SrZr}_{1-x}\text{Y}_x\text{O}_{3-\delta}$, meets water or steam, proton defects OH^- will be formed.



At high temperatures, typically above 600°C , the mobility of formed proton defects increases leading to high protonic conductivity in doped BCO/BZO⁴. In a previous study, density functional theory (DFT) calculations indicate that proton migration in the perovskite $\text{BaZr}_{0.1}\text{Ce}_{0.7}\text{Y}_{0.1}\text{Yb}_{0.1}\text{O}_{3-\delta}$ is in the form of OH^- in the presence of oxygen vacancies²¹. This means, under certain conditions, OH^- ions can also migrate in perovskite oxides.

The ionic conductivity of Y-doped SZO, $\text{SrZr}_{0.95}\text{Y}_{0.05}\text{O}_{3-\delta}$ (SZYO05) is approximately $7.0 \times 10^{-4}\text{ S cm}^{-1}$ at 600°C , which is not high enough for use as electrolyte for NAT-SOFCs²². In order to improve the ionic conductivity at low temperatures, it is necessary to increase the concentration of charge carriers, i.e., the proton defects. Therefore, we synthesized $\text{SrZr}_{1-x}\text{Y}_x\text{O}_{3-\delta}$ ($x = 0, 0.1, 0.2$) samples (Fig. 2a and Methods) and put the samples in liquid water to maximise the interaction between water and oxygen vacancies to maximise the concentration of proton defects. When the concentration of these proton defects is high enough, the neighbouring proton defects may couple or exchange with each other, in the form of H^+ or OH^- ions, forming a continuous pathway, resulting in high OH^-/H^+ ionic conductivity. It is presumed the formed proton defects may exchange charges with the neighbouring negatively charged ions such as O^{2-} ions or defects such as Y'_{Zr} to form OH^- ions. Under certain conditions, these OH^- ions may move along the pathways then the ceramic material will be an OH^- ionic conductor. The possibility of OH^- ion formation in perovskite oxides has been reported by theoretical calculations in previous studies^{23–27} although high OH^- ionic conducting ceramic materials have not been discovered yet. In this study, the high mixed OH^-/H^+ ionic conductivities in hydrated ceramic oxides SZYO20 and $\text{CaZr}_{0.8}\text{Y}_{0.2}\text{O}_{3-\delta}$ (CZYO20) are reported.

Materials characterizations of SZYO20

Based on the analysis above, it is anticipated that, doped zirconates may exhibit high ionic conductivity in water or, in the presence of high partial pressure of steam, $p\text{H}_2\text{O}$. At 100°C , the reported bulk proton conductivity of BZYO20 is in the order of 10^{-5} S cm^{-1} in air, too low to be used as an electrolyte for NAT-SOFCs¹⁵. In reported papers, at the same temperature, generally doped BZO exhibits higher ionic conductivity than doped SZO because doped BZO has a larger lattice volume thus more 'free volume' for diffusion/jumping of O^{2-} ions in the lattice^{15,22}. The diffusion of point defect protons does not require high 'free volume' but may need the right binding energy. Similar to O^{2-} ions, the diffusion of large OH^- ions also needs relatively large 'free volume'. To identify the effect of A-site ions on the ionic conductivity of Y-doped zirconates, three compounds with composition $\text{AZr}_{0.8}\text{Y}_{0.2}\text{O}_{3-\delta}$, where A = Ca, Sr, Ba were synthesized. X-ray diffraction (XRD) experiments indicate sample $\text{CaZr}_{0.8}\text{Y}_{0.2}\text{O}_{3-\delta}$ (CZYO20) is a single phase, BZYO20 has a negligible amount of reported second phase Y_2O_3 ^{28,29}, while there is a small amount of secondary phase SrY_2O_4 in SZYO20 (Supplementary Fig. 1 and Supplementary Table 1). Sample $\text{SrZr}_{0.9}\text{Y}_{0.1}\text{O}_{3-\delta}$ (SZYO10) also contains a small amount of secondary phase SrY_2O_4 indicating reducing the Y-doping level cannot eliminate it. The SrY_2O_4 secondary phase was also observed in SZYO20 when synthesised by pulsed layer deposition method³⁰ and commonly exists in Y doped perovskite oxides such as $\text{Sr}(\text{Ce}_{0.6}\text{Zr}_{0.4})_{0.8}\text{Y}_{0.2}\text{O}_{3-\delta}$ ³¹ and $\text{Sr}(\text{Ti}_{0.9}\text{Y}_{0.1})\text{O}_{3-\delta}$ ³². A possible reason is, SrY_2O_4 is a stable phase, which can be easily formed at a relatively low temperature before the formation of perovskite phase. Once it is formed, it is difficult to get rid of. The primary particle size of SZYO20 was about 200–250 nm and an agglomeration of some particles was observed by both scanning electron microscopy (SEM) and annular dark field – scanning transmission electron

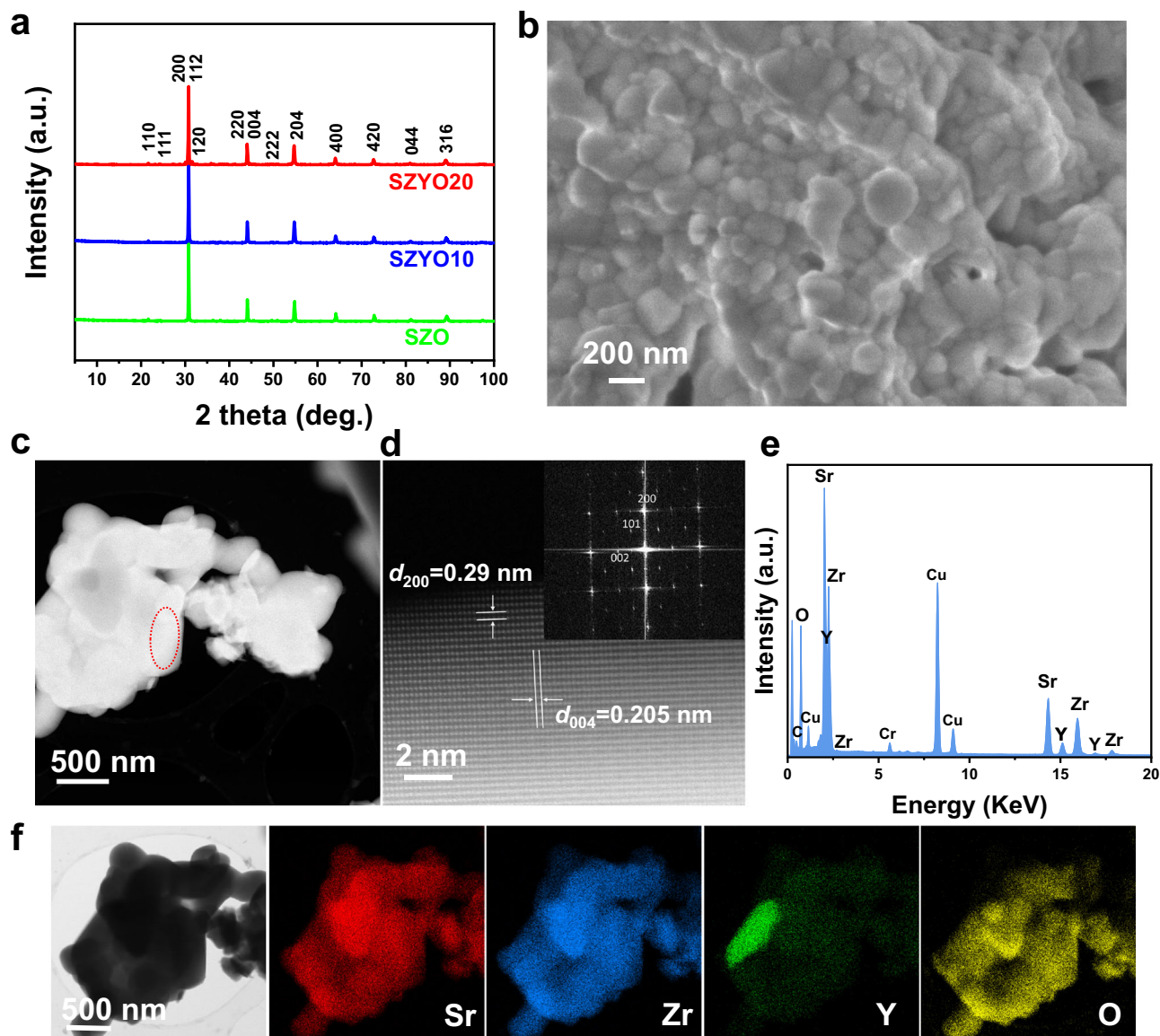


Fig. 2 | The characterizations of doped zirconates. **a** XRD patterns of $\text{SrZr}_{1-x}\text{Y}_x\text{O}_{3-\delta}$ ($x=0, 0.1, 0.2$, denoted as SZO, SZYO10, SZYO20). **b–f** SEM and TEM analysis of SZYO20 powders. **b** SEM image, **c** ADF-STEM image, **d** High-resolution ADF-STEM

image taken from marked area in (c) (inset: corresponding FFT of the image). **e** Integrated EDX spectra from the STEM-EDX analysis in (f), **f** BF-STEM image and the corresponding EDX maps of Sr, Zr, Y, O.

microscopy (ADF-STEM) (Fig. 2b, c). In Fig. 2d, the two labelled spacings were associated with the (200) and (004) lattice planes of the orthorhombic phase of SrZrO_3 (ICDD:04-014-8276), respectively. The Energy dispersive X-ray spectroscopy (EDX) elemental maps clearly show that the amount of secondary phase is small and Sr, Zr, Y and O elements are distributed evenly in the grains (Fig. 2e, f). The Y-rich area of the SZYO20 sample was confirmed to be SrY_2O_4 phase (Supplementary Fig. 2). The spacing labelled in Supplementary Fig. 2c was associated with the (200) lattice plane of the orthorhombic phase of SrY_2O_4 (ICDD:01-074-0264).

Removal of secondary phase SrY_2O_4 from the samples

It has been reported that the secondary phase of the sample, SrY_2O_4 , may react with water at high temperatures to form SrCO_3 , $\text{Sr}(\text{OH})_2 \cdot 8\text{H}_2\text{O}$ and gel phase $\text{Y}(\text{OH})_3$ ³³. Therefore, before the conductivity measurements, $\text{SrZr}_{1-x}\text{Y}_x\text{O}_{3-\delta}$ samples were heated in hot water at 90 °C for 20 h and washed three times in order to remove as much secondary phase SrY_2O_4 and the soluble hydrated product $\text{Sr}(\text{OH})_2 \cdot 8\text{H}_2\text{O}$ from the sample as possible. From STEM and EDX

analysis of pre-washed SZYO20 samples (Fig. 3a–c and Supplementary Fig. 3), the measured spacing in Fig. 3c was associated with the (002) lattice plane of the orthorhombic phase of SrZrO_3 (ICDD:04-014-8276). This indicates the perovskite phase is stable after hot water treatment at 90 °C while the secondary phase SrY_2O_4 has been almost removed. The washed sample contains ~2% SrCO_3 which is the residual product of the reaction between SrY_2O_4 and hot water³³. $\text{Sr}(\text{OH})_2 \cdot 8\text{H}_2\text{O}$ was not observed either in XRD (Supplementary Table 1) or STEM/EDX observation because it is highly soluble in water. The quantity of residual $\text{Sr}(\text{OH})_2 \cdot 8\text{H}_2\text{O}$ should be very small if there is any. In addition, STEM and EDX results indicate the presence of an amorphous material in the Y-rich area B (Supplementary Fig. 3b, c), which is likely to be $\text{Y}(\text{OH})_3$. This amorphous material stays on the grain boundary or presents as isolated particles among perovskite particles (marked area in Fig. 3a). The elemental analysis of SZYO20 samples before and after being washed in hot water indicated that, the Sr-content slightly decreased for the washed sample, confirming the soluble hydrolysis products $\text{Sr}(\text{OH})_2 \cdot 8\text{H}_2\text{O}$ had been successfully removed (Supplementary Table 2). The hydrolysis of SrY_2O_4 at 90 °C was also confirmed by XRD

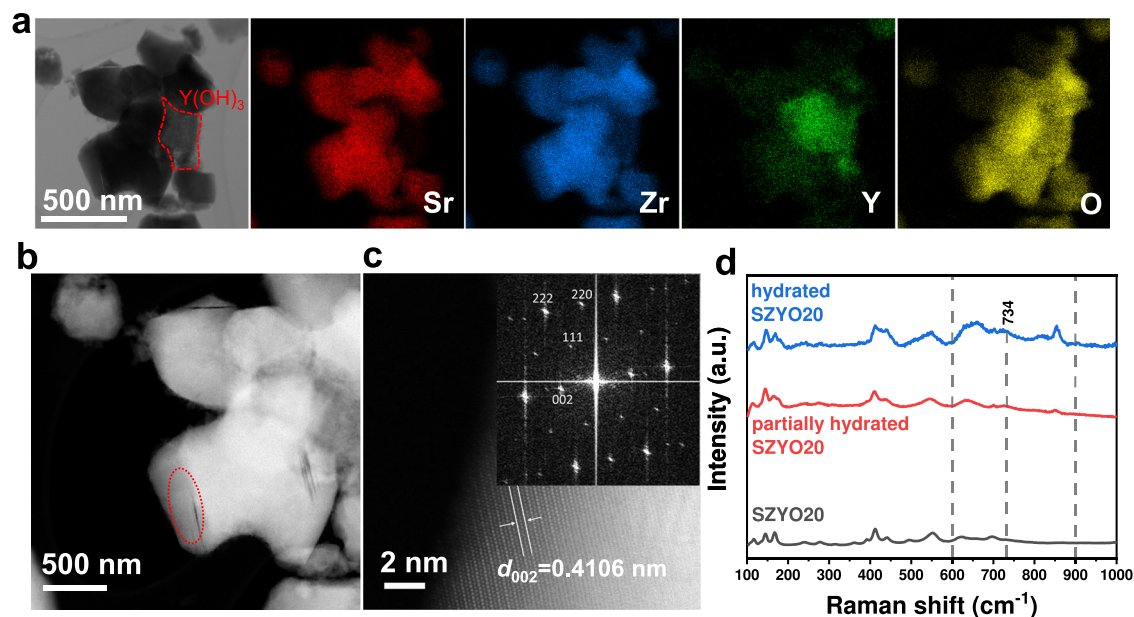


Fig. 3 | TEM and Raman characterizations of washed SZYO20. **a–c** TEM analysis of washed SZYO20 powders. **a** BF-STEM image and the corresponding EDX maps of Sr, Zr, Y, O, **b** ADF-STEM image, **c** High resolution ADF-STEM image taken from

marked area in **(b)** (inset: corresponding FFT of the image). **d** Raman spectra of SZYO20 samples with different hydration levels.

analyses (Supplementary Fig. 4). All samples for conductivity measurements were treated in water at 90 °C for 20 h (repeated three times) to remove as much SrY_2O_4 as possible to minimise the possible contribution of SrY_2O_4 and its hydrolysed product $\text{Sr}(\text{OH})_2 \cdot 8\text{H}_2\text{O}$ on the measured conductivity. However, we do not rule out that the trace residual $\text{Sr}(\text{OH})_2$ from hydrolysis of SrY_2O_4 may provide feeding OH^- ions to SZYO20, which contributes to the conductivity to some extent.

Importance of hydration and conductivity measurement

The measurement of traditional protonic conducting perovskite oxides such as doped zirconates or cerates are normally measured in wet air or wet H_2 , passing the gas through room temperature water with the steam partial pressure of 0.03 bar, i.e., 3 mol% steam in the humidified air or hydrogen. The measured conductivity at NAT is very low¹⁵. According to our analysis above (Fig. 1 and Eq. 1 & 2), the water or steam concentration mentioned in reported papers may not be enough to form sufficient proton defects in order to form continuous pathways for OH^-/H^+ ions. Therefore, we decided to directly measure the conductivity and ion transfer number of the prepared and pre-washed $\text{AZr}_{0.8}\text{Y}_{0.2}\text{O}_{3-\delta}$ ($A = \text{Ca}, \text{Sr}, \text{Ba}$) pellets in water (Supplementary Fig. 5), which is the method commonly used for conductivity measurement in polymeric alkaline membranes¹⁷. In our study, at room temperature, the conductivity of un-washed SZYO20 pellet in water kept increasing against time (Supplementary Fig. 6). It increased from $2.96 \times 10^{-4} \text{ S cm}^{-1}$ to $2.28 \times 10^{-3} \text{ S cm}^{-1}$ in 10 h indicating hydration of the oxide to form proton defects is very important in order to achieve high ionic conductivity (Eq. 2). After aging in water at room temperature, the ionic conductivity of SZYO20 in water, is already higher than the protonic conductivity of SZYO05, $7.0 \times 10^{-4} \text{ S cm}^{-1}$, at 600 °C when measured in H_2 ²². The conductivity of pure SrY_2O_4 in water at room temperature remains around $1.7 \times 10^{-4} \text{ S cm}^{-1}$ against time, only -7.5% of that for fully hydrated SZYO20 (Supplementary Fig. 6c), indicating the increased conductivity of the un-washed SZYO20 is mainly due to the hydration of SZYO20, or in other words, the interaction between SZYO20 and liquid water. This experiment indicates it is difficult to discover the real high ionic conductivity of hydrated SZYO20 if the duration of submerging the pellet in water is not long enough.

To rule out the possible contribution of residual Y_2O_3 or $\text{Y}(\text{OH})_3$ in the pre-washed SZYO20 sample, conductivities of pure Y_2O_3 and $\text{Y}(\text{OH})_3$ in water were measured indicating they have very low ionic conductivity, in the range of $10^{-5} - 10^{-4} \text{ S cm}^{-1}$ at 90 °C in water (Supplementary Fig. 7). This means the observed Y-rich phase in STEM (Fig. 3a) will have little contribution to the observed overall high ionic conductivity of SZYO20 at elevated temperatures.

The interaction between oxygen vacancies and water was also confirmed by Raman spectra (Fig. 3d). The peaks in the 600–900 cm^{-1} region are slightly wider when the SZYO20 sample is wetter. When the hydration level of SZYO20 sample is higher, the Raman peak shifts towards higher values (734 cm^{-1}), which is consistent with the Raman features of proton insertion in oxygen vacancies in Yb-doped SZO and BZO³⁴.

The jumping or diffusion of ions in a lattice, is not only related to the high concentration of proton defects and the formed OH^- species when it is heavily hydrated, but also to the mobility of ions in a given lattice, and in some cases, this is correlated with the ‘free volume’ (for large OH^- ions) and jumping distance between neighbouring available sites (Fig. 1). In general, larger lattice parameters or bond lengths results in higher ‘free volume’, which may help to reduce the transition barrier of ionic diffusion, therefore favouring the mobility of large OH^- ions, while longer jumping distance for ions will reduce the mobility. These two effects are opposite on the ionic conductivity. Therefore, there must be an optimal lattice size, which compromises between ‘free volume’ and jumping distance, exhibiting the highest ionic conductivity. It was found that sample SZYO20 exhibits the highest ionic conductivity in the $\text{AZr}_{0.8}\text{Y}_{0.2}\text{O}_{3-\delta}$ ($A = \text{Ca}, \text{Sr}, \text{Ba}$) series (Fig. 4a and Supplementary Fig. 8), which is consistent with the observed proton conductivity of $\text{AZr}_{0.95}\text{In}_{0.05}\text{O}_{3-\delta}$ ($A = \text{Ca}, \text{Sr}, \text{Ba}$) in H_2 at a temperature of 600 – 1000 °C in which $\text{SrZr}_{0.95}\text{In}_{0.05}\text{O}_{3-\delta}$ exhibits the highest conductivity⁸. There is also a possibility that mobile ions like OH^- diffuse through the grain boundary to promote ionic conductivity. To understand whether the ion transfer in both bulk and grain boundaries contributes to the conductivity, electrochemical impedance spectrum (EIS) was acquired up to a high frequency of 10 MHz, and equivalent electrochemical circuits were fitted and simulated to extract the bulk

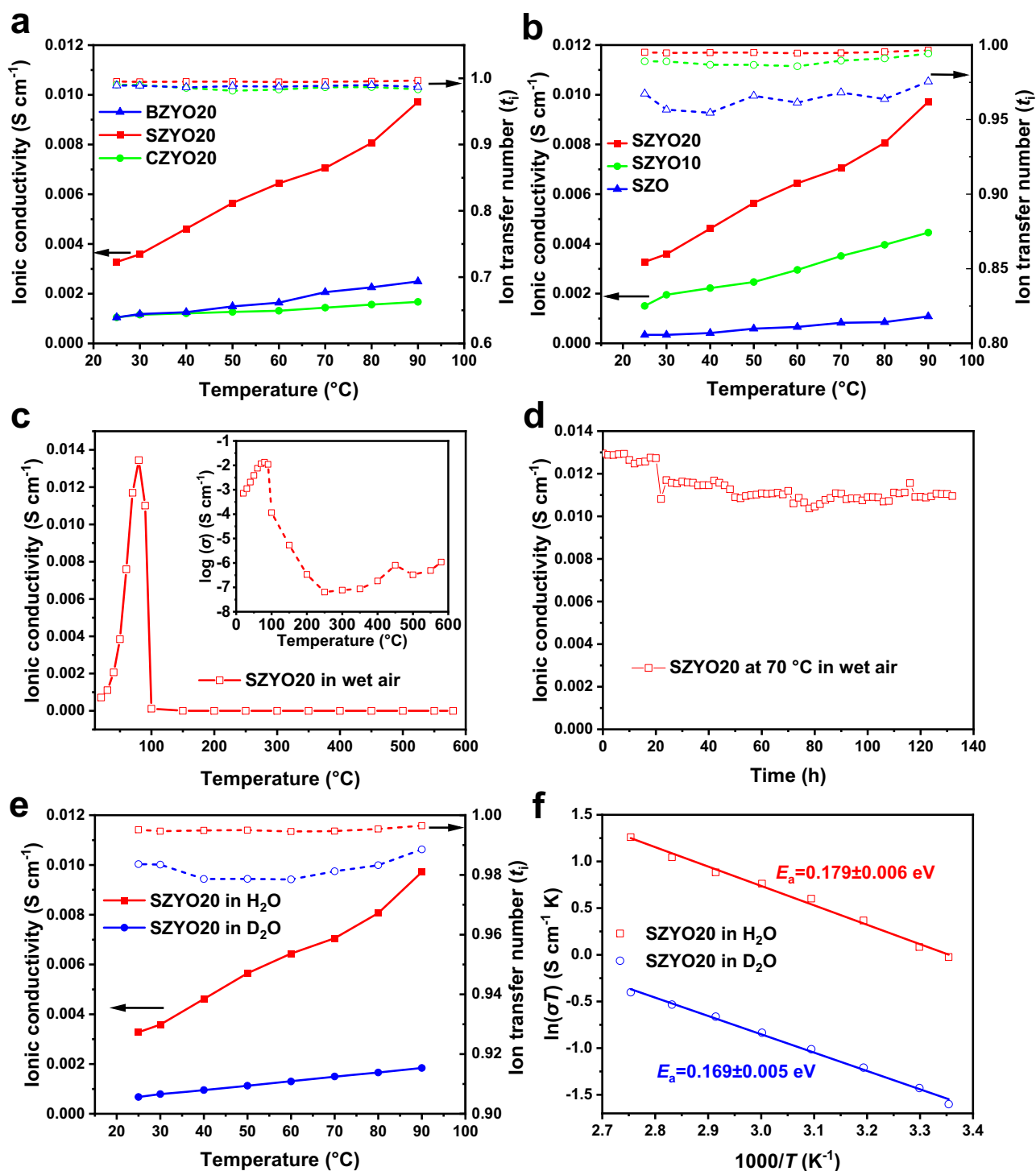


Fig. 4 | The ionic conductivity of doped zirconates under different conditions. **a** $AZr_{0.8}Y_{0.2}O_{3-\delta}$ ($A = Ca, Sr, Ba$, denoted as CZYO20, SZYO20, BZY020), measured in water. **b** $SrZr_{1-x}Y_xO_{3-\delta}$ ($x = 0, 0.1, 0.2$, denoted as SZO, SZYO10, SZYO20),

measured in water. **c** SZYO20 in wet air at different temperatures. **d** Stability of the conductivity of SZYO20 in wet air at 70 °C. **e**, **f** Conductivity (**e**) and activation energy (**f**) of SZYO20 in H_2O and D_2O .

and grain boundary resistances. In order to observe a complete grain boundary response, the impedance spectrum was also recorded at $-25^\circ C$ (Supplementary Fig. 9). All the impedance dataset was validated by performing Kramers-Kronig analyses, i.e., the real and imaginary residuals are lower than 1%^{35,36}. It is interesting that at $-25^\circ C$ the bulk conductivity of BZY020 is the highest as expected due to its larger lattice volume, but when the conductivity test temperature reached room temperature and above (i.e., liquid water environment), not only

the grain boundary conductivity but also the bulk conductivity of SZYO20 increases rapidly, both of which contribute to the highest total conductivity among the three $AZr_{0.8}Y_{0.2}O_{3-\delta}$ ($A = Ca, Sr, Ba$) oxides (Supplementary Fig. 8c, d). This shows to a certain extent that the conductive ions not only diffuse in the perovskite lattice but may also transport through the grain boundaries. After hydration, the presence of hydrogen and additional oxygen atoms from hydroxide filling vacancies in the bulk of SZYO20 has been identified in later neutron

diffraction discussions, which verified the bulk diffusion occurring in the perovskite lattice. On the other hand, although we believe the very trace amounts of $\text{Sr}(\text{OH})_2$ and $\text{Y}(\text{OH})_3$ residues in the washed sample are not enough to directly provide sufficient conductivity, we do not rule out that the free unbonded proton and OH^- ions in the environment use their O-H channels to transport across the grain boundaries and therefore contribute to a high conductivity of SZYO20. At high temperatures, the reported proton conductivity in doped BZO is generally higher than that of doped SZO. However, when the conductivity of these oxides was measured in water, in the $\text{AZr}_{0.8}\text{Y}_{0.2}\text{O}_{3-\delta}$ (A = Ca, Sr, Ba) series, it is SZYO20 that exhibits the highest ionic conductivity. This implies the charge carriers may not be protons or may not be dominated by protons. When the charge carriers are different, the conduction mechanism could be different thus may not necessarily follow the mechanism for proton diffusion/jumping at high temperature. Actually, in our later concentration cell measurements, it has been demonstrated that heavily hydrated SZYO20 is a mixed OH^-/H^+ conductor while OH^- ions are the dominant charge carrier (Supplementary Table 3). This is very different from the previously reports that, at high temperature, doped BZO and SZO are proton conductors. The same materials, when exposed to different environments, can have distinct charge carriers which contribute to the conductivity.

A low temperature concentration cell measurement was applied to determine which charge carriers are the conduction ions (Supplementary Fig. 10 and Supplementary Note 1)³⁷. According to the measured ion transport number of SZYO20, at room temperature, about 70% of the measured ionic conductivity is due to the transfer of OH^- ions (Supplementary Table 3). The proton transference number was determined to be -0.27 at room temperature (Supplementary Fig. 11), which is consistent with the cation transport number measured by the concentration cell. This indicates heavily hydrated SZYO20 is a mixed OH^-/H^+ ion conductor and predominantly presents OH^- conduction, which is very different from the previous knowledge of conventional doped zirconates, which are considered as mixed H^+/O^{2-} ionic conductors above 500 °C depending on the temperature range³⁸. In this study, it has been observed that, not only protons but OH^- ions may also jump or diffuse via the oxygen vacancies or proton defects after hydration with liquid water. Hydroxide ionic conduction was also previously proposed in similar perovskite oxides $\text{SrCe}_{0.95}\text{Yb}_{0.05}\text{O}_{3-\delta}$ (SCYb) and $\text{BaCe}_{1-x}\text{Gd}_x\text{O}_{3-\delta}$ (BCG) in the presence of water vapour at high temperature (> 500 °C) while the observed ionic conduction was very low because $p\text{H}_2\text{O}$ is not high enough^{23,39}. The reason for this difference is, the conductivity is measured under different conditions. The ionic conductivity of SZYO20 in this study was measured in water or heavily humidified gas (passing air through boiling water at 100 °C) while in previous studies, the conductivity was typically measured in an atmosphere passing room temperature water, as stated above.

In most oxides that are high temperature mixed O^{2-}/H^+ ionic conductors, such as the doped BZO/BCO perovskites, oxygen vacancies play a critical role for high ionic conductivity¹. To determine the role of oxygen vacancies on the resulting high ionic conductivity of SZYO20, SZO and SZYO10 were also synthesised. XRD results indicate that SZO is a single phase, while SZYO10 contains a small amount of secondary phase SrY_2O_4 (Supplementary Figs. 1c, 12). Both SZO and SZYO10 were pre-washed at 90 °C in water for three times to remove any soluble impurities and minor SrY_2O_4 secondary phase. As shown in Fig. 4b, among the three oxides, the order of conductivity and ionic transfer number is $\text{SZYO20} > \text{SZYO10} > \text{SZO}$. This is because SZYO20 has the highest doping level thus the highest concentration of oxygen vacancies (Eq. 1), thus more proton defects (Eq. 2), which means there will be more OH^- species formed through charge exchange with neighbouring negatively charged O^{2-} ions or Y'_{Zr} defects, leading to the highest ionic (both OH^- and H^+ ions) conductivity. The same phenomenon was observed in Y doped BZO and CaZrO_3 (CZO). For oxides with negligible or no secondary phases, such as BZO, BZY020, CZO,

CZY020, the conductivity of the Y-doped oxides in water is much higher (approximately 6 times) than that of un-doped ones (Supplementary Fig. 13a–d). This indicates the importance of extrinsic oxygen vacancies in order to achieve high ionic conductivity in water. It can be reasonably deduced that the high ionic conductivity is mainly due to the deliberately introduced extrinsic oxygen vacancies through Y-doping, rather than the residual $\text{Sr}(\text{OH})_2 \cdot 8\text{H}_2\text{O}$. In addition, it is worth noting that, without SrY_2O_4 secondary phase, the conductivity of pure SZO is also high, exhibiting the highest conductivity among AZrO_3 (A = Ca, Sr, Ba) as shown in Supplementary Fig. 13e, which means SZO is the lattice with optimised 'free volume' and jumping distance for OH^- ions. It is possible there could be a small amount of intrinsic oxygen vacancies in the fired pure oxides such as CZO/SZO/BZO, which allows the formation of proton defects according to Eq. 2 and the diffusion of generated OH^- ions. However, we cannot completely rule out the possibility that the alkaline elements Ca, Sr or Ba in the perovskite might slowly dissolve in water to form metal hydroxide contributing to the measured conductivity of the oxides. Therefore, we measured the pH value and conductivity of the water used in the conductivity measurement, immediately after the completion of ionic conductivity measurement by a.c. impedance. The conductivity of the used water is always much lower than the measured conductivity of pellets except for BZO which has the lowest conductivity in water (Supplementary Table 4). For SZYO20, at room temperature, the total conductivity of used water was $407.1 \mu\text{S cm}^{-1}$, which is only 19% of the total conductivity of SZYO20 pellet, $2174.98 \mu\text{S cm}^{-1}$. The contribution of any species from slow dissolution of the perovskite in water to the measured total conductivity of SZYO20 is negligible. Therefore, the majority of the measured conductivity of the oxide pellets is from the hydrated oxide itself while any other species from the dissolved perovskite oxide in water may have a small contribution to the measured total conductivity, presuming water with the dissolved species enters the pores of the oxide pellets.

In water, the ionic conductivity of sample SZYO20 is $3.28 \times 10^{-3} \text{S cm}^{-1}$ at 25 °C, and $9.71 \times 10^{-3} \text{S cm}^{-1}$ at 90 °C respectively with ion transfer numbers higher than 0.995 (Fig. 4a). This indicates it is a predominantly ionic conductor when exposed in water. This is consistent with the knowledge of solid state ionic conductors as there are no multi-valent elements in these oxides. The ionic conductivity and transfer number of SZYO20 is sufficient to be used as electrolytes for fuel cells and electrolyzers at 90 °C when thin-film technology used for conventional SOFCs is applied¹. When only considering its ability to transport hydroxide ions, the OH^- conductivity of SZYO20 is close to that of some polymer-based alkaline membranes as shown in Supplementary Table 5.

For fuel cell applications, the cathode side may be exposed to humidified O_2 or humidified air such as conventional PEMFCs based on acidic Nafion membrane electrolyte. Therefore, it is very important to measure the ionic conductivity in humidified air. In conventional proton conductivity measurements, the samples are passing through room temperature water with ~3% water vapour. In our study, air was passing through 100 °C boiling water in order to fully humidify the oxides. The real temperature of the oxide pellet was recorded by a thermocouple next to the sample. At 90 °C, the conductivity of SZYO20 in as-humidified air is $1.1 \times 10^{-2} \text{S cm}^{-1}$ while it suddenly drops at above 100 °C (Fig. 4c and Supplementary Fig. 14a–c). This means the high ionic conductivity of SZYO20 is related to the presence of liquid water either in pure water or a mixture of liquid water and steam as the case of humidified air by passing air through 100 °C boiling water. At 70 °C, the conductivity of SZYO20 in wet air is stable at 0.01S cm^{-1} for the measured 130 h (Fig. 4d), which is reflected in the a.c. impedance spectra (Supplementary Fig. 14d, e). This indicates the ceramic ionic conductor SZYO20 has excellent stability in humidified air. After conductivity measurements, the chemical composition was still perovskite oxide, confirmed by both XRD and element mapping

(Supplementary Fig. 15). Pre-washed SZYO20 sample contains 2% residual SrCO_3 due to hydrolysis of second phase SrY_2O_4 and the SrCO_3 remains 2% in SZYO20 sample after conductivity measurement in humidified air at 70 °C for 130 h indicating excellent chemical compatibility with CO_2 in air. If there is any residual SrY_2O_4 , it may hydrolyse to form $\text{Sr}(\text{OH})_2 \cdot 8\text{H}_2\text{O}$ during the conductivity stability measurement then the yielded $\text{Sr}(\text{OH})_2 \cdot 8\text{H}_2\text{O}$ may further react with CO_2 in humidified air to form SrCO_3 , leading to increased SrCO_3 . The consistency of SrCO_3 content before and after the conductivity measurement indicates there is negligible residual SY_2O_4 or $\text{Sr}(\text{OH})_2 \cdot 8\text{H}_2\text{O}$ in the pre-washed sample.

The excellent chemical stability of SZYO20 in humidified air is anticipated. It is well-known that BZY020 is a stable proton conductor, which has been widely investigated as electrolyte for SOFCs, due to its excellent chemical stability in steam and CO_2 ^{16,40}. Theoretically, in AZrO_3 where A = Ca, Sr, Ba, the order of chemical stability is $\text{BZO} < \text{SZO} < \text{CZO}$ because the large Ba^{2+} ions are the most polarised while the small Ca^{2+} ions are the least polarised. From this point of view, SZYO20 should exhibit higher chemical stability than BZY020. This is consistent with the observed excellent chemical stability of SZYO20 in humidified air, which means 'free' air can be directly used as the oxidant in fuel cells when humidified SZYO20 is used as the electrolyte. In conventional alkaline fuel cells based on KOH solution electrolyte or, polymeric alkaline membrane fuel cells based on quaternary ammonium groups, air cannot be directly used as the oxidant at the cathode of alkaline fuel cells (AFCs) or alkaline membrane fuel cells (AMFCs) because CO_2 may react with KOH to form K_2CO_3 which may block the holes in electrode in AFCs or, react with polymeric alkaline membrane with significantly reduced OH^- ionic conductivity in AMFCs. The discovery of high OH^- ionic conductivity in ceramic oxide SZYO20 will provide a low temperature OH^- ionic conductor to be used as electrolyte for low temperature fuel cells such as NAT-SOFCs or electrolyzers for splitting of water for hydrogen production. This eliminates the problem of poor CO_2 compatibility of the electrolyte in AFCs and AMFCs.

Kinetic isotope effect

For proton conducting materials, the conductivity in D_2O will be reduced due to the decreased mobility of D^+ ions^{8,41}. This is also called the kinetic isotope effect (KIE). The conductivity of SZYO20 in pure D_2O was also measured to investigate its effect on proton conduction (Fig. 4e). At 90 °C, the conductivity in H_2O is 5.28 time of that in D_2O , which is reflected in the a.c. impedance spectra in Supplementary Fig. 16. For pure proton conductors, the KIE is usually no less than 1.4 for Grotthuss mechanism, while it is close to 1.2 for vehicle mechanism⁴¹. As the KIE is much larger than 1.4, it is presumed that SZYO20 is not a pure protonic conductor. This is consistent with the ion transfer number measured through concentration cell, i.e., 70% of the charge carriers are OH^- ions. Similarly, in a previous report, the observed OH^- ionic conduction in the perovskite oxides SCYb and BCG in the presence of water vapour does not follow the kinetic isotope effect either^{23,39}.

The large difference between the conductivity in H_2O and D_2O , implies the large OH^- ions are the major charge carriers, while jumping or diffusion of large OD^- ions could be more difficult than that for OH^- ions. The activation energy of SZYO20 in H_2O and D_2O was 0.179 ± 0.006 eV and 0.169 ± 0.005 eV respectively (Fig. 4f). It is close to the 0.17 eV for Nafion membrane in H_2O ⁴¹ and within the range of activation energy for OH^- conducting polymers (0.12–0.26 eV)⁴². The activation energy of doped SZO at low temperature (< 100 °C) in this study is very different to that reported for doped SZO at high temperature with the range of 0.4–0.6 eV at 700–1000 °C when the dominant charge carriers are H^+ and O^{2-} ions²². This indicates the charge carriers in liquid water may be different, predominantly OH^- ions. This explains why the hydrated SZYO20 is a mixed OH^-/H^+

conductor, while the transfer number for OH^- ions is much higher than that for cations, H^+ ions (Supplementary Table 3).

The particle size remained unchanged after sample SZYO20 had been measured in water, D_2O or wet air (Supplementary Fig. 17), further confirming the excellent chemical stability of SZYO20.

Solid state NMR measurements

In order to further investigate the conduction mechanism of SZYO20 in water, solid-state nuclear magnetic resonance (NMR) has been employed to study the dry and partially hydrated SZYO20. Figure 5a shows the solid state ^1H NMR spectra of dry (red) and partially hydrated (blue) SZYO20. The ^1H spectrum of dry SZYO20 shows three resolved signals at 4.4, 3.5 and 0.7 ppm that can be assigned to H_2O , OH^- groups bound on defects or surface and, H^+ bound to oxygen of the Sr-O-Y or Sr-O-Zr environments, respectively. Akin assignments of proton signals on similar samples have been reported^{43–45}. As the sample gets partially hydrated the ^1H signal increases dramatically and shows two broad peaks at 4.6 and 2.3 ppm which can be assigned to water at 4.6 ppm and to signals from OH^- and H^+ moieties and their exchange at 2.3 ppm. The deconvolution of the partially hydrated sample is shown on Supplementary Fig. 18. The fast MAS experiments were performed with a 1.3 mm probe that has limited variable temperature capabilities. Figure 5b shows the solid state ^1H NMR (MAS 60 kHz) spectra of partially hydrated (top) and dry (bottom) SZYO20 measured with the sample at –5 °C (blue) and +30 °C (red). On both samples, the water peak shifts slightly with the temperature (approximately 0.1 ppm / 10 °C)⁴⁶. At both temperatures, the dry and the wet samples, the signals assigned to OH^- and to H^+ are getting broader as the temperature increases which suggests the presence of exchange between the two moieties. ^1H nuclear overhauser effect spectroscopy (NOESY) spectra of the dry and hydrated samples are shown in Fig. 5c, d and prove proximity between different ^1H moieties.

To further investigate the temporary formation of hydrogen bond and its disappearance above 100 °C, the ^1H MAS spectra at 25, 95 and 125 °C on partially hydrated SZYO20 were recorded with a 1.6 mm HXY Phoenix NMR probe spinning at 30 kHz (Supplementary Fig. 19). The sample used for high temperature measurements was slightly less hydrated than the one used to record the ^1H spectra shown in Fig. 5a such that the peak at 0.7 ppm is visible on the partially hydrated sample. At higher temperatures the intensity of this peak, assigned to H^+ , increases and clearly becomes narrower at above 100 °C. At 125 °C the position of the peak is slightly shifted to 0.8 ppm. This shift can be clearly identified on the spectra measured at 95 °C when probably two forms of H^+ , one that is bound (0.7 ppm) and one that is more mobile (0.8 ppm), coexist. This means that there will be more mobile H^+ ions in SZYO20 at 125 °C compared to that at 95 °C. The more the free unbounded H^+ ions, the fewer hydrogen bonds. The hydrogen bonds mean both the hydrogen bonds to the neighbouring oxygen in a water molecular and a lattice oxygen from the perovskite oxide. On the other hand, the peak at 2.3 ppm assigned to signal from OH^- and H^+ exchange partially splits to peaks at 3.8 ppm and 0.8 ppm at 125 °C as indicated in Supplementary Fig. 19. Considering the peak shift at higher temperatures and error bars for measurements (± 0.1 or so ppm), this is consistent with the signals at 3.5 ppm and 0.7 ppm for dry samples and signal at 2.3 ppm for partially hydrated sample measured at room temperature (Fig. 5a), indicating the conversion of SZYO20 sample from hydrated to dry level when temperature increases to over 100 °C, representing the conversion of OH^- and H^+ moieties in full exchange to part exchange then to no exchange. This is consistent with the low conductivity of SZYO20 when the temperature is above 100 °C at ambient pressure, which is because in the absence of liquid water, it is hard to facilitate the hydrogen bond formation to diffuse OH^- ions.

We have also performed ^{89}Y MAS NMR experiments on the partially hydrated sample as shown on Fig. 5e. The ^{89}Y direct polarisation (DP) signal measured with a spin echo experiment shows two broad

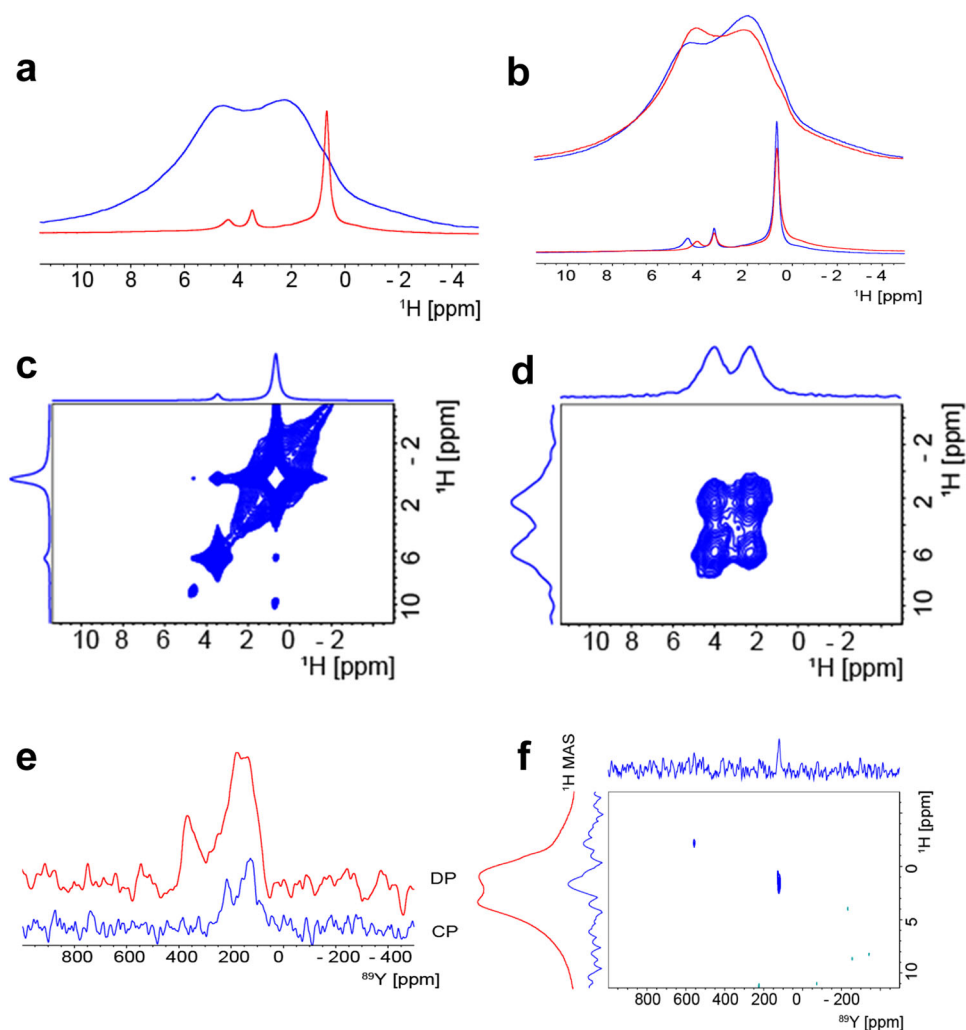


Fig. 5 | Solid state NMR spectra of dry and partially hydrated SZYO20. **a** The solid state ^1H NMR spectra of dry (red) and partially hydrated (blue) SZYO20. **b** The solid state ^1H NMR (MAS 60 kHz) spectra of partially hydrated (top) and dry (bottom) SZYO20 performed with the rotors kept at -5°C (blue) and $+30^\circ\text{C}$ (red). **c, d** ^1H - ^1H NOESY correlation spectra (MAS 60 kHz) of dry (c) and partially hydrated

(d) SZYO20 mixing time (c) 0.1 s and (d) 1 s. **e** ^{89}Y MAS at 8 kHz DP spectrum measured with a spin echo (red) and cross polarisation (blue) from ^1H of partially hydrated SZYO20. **f** ^1H - ^{89}Y heteronuclear correlation experiment obtained with 6 ms cross polarisation, MAS 8 kHz.

signals at 370 and 160 ppm indicating Y sites are coordinated by 6, 7 and 8 oxygen atoms^{24,47}. The ^1H - ^{89}Y cross polarisation (CP) spectrum shows two ^{89}Y signals at 219 and 130 ppm (mainly 7 and 8 coordinated sites) in proximity to ^1H nuclei. The ^1H - ^{89}Y heteronuclear correlation experiment, performed on the partially hydrated sample is displayed in Fig. 5f. It shows that the ^{89}Y signals correlates with the ^1H signal at 2.3 ppm which we assign to the OH^- and H^+ exchange signal. This indicates the mobile OH^- and H^+ ions are associated with Y^{3+} sites since Y^{3+} doping introduces oxygen vacancies in the SZO lattice, as shown in Eq. 1 and Eq. 1. This is also consistent with the Raman results (Supplementary Fig. 20 and Supplementary Note 2). In water, the real composition of hydrated $\text{SrZr}_{1-x}\text{Y}_x\text{O}_{3-\delta}$ is hydrated or unhydrated oxyhydroxide, with a general formula, $\text{SrZr}_{1-x}\text{Y}_x\text{O}_{3-\delta-y}(\text{OH})_{2y+z}\cdot z\text{H}_2\text{O}$ ($= \text{SrZr}_{1-x}\text{Y}_x\text{O}_{3-\delta}n\text{H}_2\text{O}$, $n=y+z$), where the upper limit for y is the oxygen deficiency δ . With $y=\delta$ reflecting a hydrogen content consistent with complete filling of the oxygen vacancies. For $z=0$, it is unhydrated oxyhydroxide while for $z>0$, it is hydrated oxyhydroxide. The OH^- ions are presented in the form of protonic defects, OH_0^\bullet , which are associated with oxygen vacancies. These proton defects may further form OH^- species through charge exchange with neighbouring negatively charged species. The exchange and coupling of OH^- and

H^+ ions in hydrated SZYO20 nearby Y^{3+} ions has been confirmed by solid-state NMR observation which helps us for a better understanding of the conduction mechanism of SZYO20 in water.

To further confirm the existence of hydrogen and hydrogen-related species such as OH^- ions in the perovskite oxide, the same solid-state ^1H and ^{89}Y NMR experiments were also carried in CZYO20 powders. As shown in Supplementary Fig. 21a, the DP ^{89}Y MAS spectrum of water-hydrated CZYO20 is comparable with the ^{89}Y spectra of partially hydrated SZYO20, but the signal at 200 ppm is narrower and does not extend over the 160 ppm region where the ^{89}Y signal of the ^1H - ^{89}Y CP spectrum of SZYO20 shows higher coordination ^{89}Y in proximity with ^1H . For CZYO20, the ^1H fast MAS spectra shown in Supplementary Fig. 21b and the ^1H NOESY correlations shown in Supplementary Fig. 21c, d are comparable with the ^1H spectra of SZYO20 with the similar composition shown in Fig. 5a-d, but the signal we assigned to OH^- is much broader and distributed over a larger frequency range. Based on the chemical composition of hydrated oxides, we believe both H^+ and OH^- ions co-exist in hydrated perovskite oxides. Under certain conditions, theoretically both ions can diffuse in the oxide lattice, forming a mixed OH^-/H^+ ionic conductor.

TG and raman spectra analysis

Simultaneous Thermal Analysis (STA) was carried out on partially hydrated SZYO20. According to the Differential Scanning Calorimetry (DSC) and Thermogravimetry (TG) curves in Supplementary Fig. 22, the weight loss gradually increases with temperature. The weight loss detected below 100 °C is from physically absorbed water and gases, which is not used for the hydration analysis. Chemically bound water associated with the carbonate traces present on the sample surface normally contributes to the loss observed at about 300 °C³⁴, which is also the temperature at which OH⁻ in perovskite-like hydroxides usually departs^{48,49}. The weight loss step observed between 800 and 850 °C in Supplementary Fig. 22a is assigned to the departure of protonic species associated with conductive properties which has been reported for other similar oxides^{34,48}. According to the oxygen occupancy parameters obtained by the XRD Rietveld refinement for SZYO20 samples (Supplementary Table 1), the oxygen vacancies are mainly at the O2 sites and the total oxygen concentration in the perovskite *Pbnm* phase is 2.928 (~2.93), thus the investigated perovskite phase can be written as SrZr_{0.86}Y_{0.14}O_{2.93}. This is also consistent with the oxygen occupancy obtained in neutron diffraction analysis, implying ~2.4% oxygen vacancies ($\delta = 0.07$) in the unhydrated SZYO20 (Supplementary Table 6). The Zr/Y atomic ratio of washed SZYO20 obtained by STEM-EDX (Supplementary Table 2) is close to and slightly lower than the Zr/Y atomic ratio of precise SrZr_{0.86}Y_{0.14}O_{2.93} phase. Therefore, it is reasonable to speculate that except for a tiny amount of Y-rich residues, the perovskite phase SrZr_{0.86}Y_{0.14}O_{2.93} is still stably retained in the washed samples, possibly forming the hydrated oxyhydroxide SrZr_{0.86}Y_{0.14}O_{2.86}(OH)_{0.14}·*n*H₂O. Theoretically, the OH⁻ species in this oxyhydroxide would completely decompose before 850 °C as the weight of the sample became stable above this temperature. Therefore, the water content *n* in hydrated oxyhydroxide SrZr_{0.86}Y_{0.14}O_{2.93}·*n*H₂O is estimated to be *n* = 0.552. Similarly, for water-hydrated CZYO20, the TG curve plateaus above 695 °C (Supplementary Fig. 22b) thus the water content *n* in CaZr_{0.8}Y_{0.2}O_{2.9}·*n*H₂O is estimated to be *n* = 0.065. This is consistent with what was observed in the conductivity measurement (Fig. 4a), i.e., the ionic conductivity of CZYO20 is much lower than SZYO20 in water because the water content in hydrated CZYO20 is much smaller and is fully dehydrated at a lower temperature compared to hydrated SZYO20. This further demonstrates the importance of hydrated water in order to achieve high ionic conductivity.

The loss of hydrogen bonds and OH⁻ species in hydrated oxides at high temperatures is further confirmed by the in situ high temperature Raman spectra shown in Supplementary Figs. 23, 24, which were measured on heating from 22 °C to 1000 °C. Supplementary Fig. 23a shows the spectra associated with the vibrational dynamics of the SZYO20 oxide lattice. It has been reported that intercalation of water fills vacancies in the lattice, thus resulting in less peak splitting in the spectrum^{34,50}. A slight broadening of bands is observed from 150 °C to 400 °C. After further thermal dehydration, the Raman features in 400–900 cm⁻¹ region slightly shift to a lower wavenumber, and a new peak is formed at 820 cm⁻¹ at temperatures above 800 °C, suggesting the removal of protons from oxygen vacancies³⁴ and a phase transition away from the hydrated structure⁴⁸. The peaks above 3600 cm⁻¹ in Supplementary Figs. 23b, 24b are assigned to the hydroxyl (OH⁻) groups formed in the perovskite oxide upon hydration^{50–52}. These peaks almost disappear at above 300 °C indicating the departure of OH⁻. The extra peak at 469 cm⁻¹ in Supplementary Fig. 24a for water-hydrated CZYO20 can also be assigned to a vibration related to oxygen vacancies filled with hydroxyl groups⁵², which disappear at above 600 °C, consistent with the TG analysis.

Neutron diffraction analysis

Due to a lack of sensitivity of X-ray scattering to protons and oxygen atoms in metal oxides, the proton positions and oxygen occupancy of

the water-hydrated sample could not be precisely refined by XRD. In order to identify the position of OH⁻ and/or hydrogen in the structure and more reliably determine oxygen positions, neutron diffraction data was collected on deuterated samples. The washed SZYO20 powder was further hydrothermally deuterated at 225 °C for 12 h prior to neutron diffraction measurement (Supplementary Note 3). The deuterated sample was not found to contain secondary SrY₂O₄ phase or residual Sr(OH)₂·8H₂O, while some Y(OH)₃ (6.9% phase fraction) was found to be present, which corroborates with the Y-rich area observed in the STEM analysis of the washed sample (Fig. 3a). The mixed Zr/Y site occupancies were not able to be reliably refined as they have very similar neutron scattering lengths (Zr 7.16 fm, Y 7.75 fm)⁵³. Y(OH)₃ has very low solubility in water, therefore an overall Zr:Y ratio of 4:1 for the total deuterated sample was used to calculate the stoichiometry of the perovskite phase SrZr_{1-x}Y_xO_{3- δ} . A value of *x* = 0.14 for the yttrium concentration was calculated which was used for the subsequent refinements. Refinement of the strontium positions for deuterated SZYO20 were not found to significantly differ from the anhydrous structure (Supplementary Fig. 25 and Supplementary Tables 6, 7). The strontium site occupancy was refined to a value very close to one and was therefore fixed to a value of one. Refinement of the oxygen occupancies were found to converge towards unity, consistent with uptake of OD into vacancies. Deuterium was found to stably refine to a position of (0.663(6), 0.158(6), 0.042(4)), with a corresponding decrease in the goodness of fit and the standard uncertainties of the refined parameters after the addition of D in the structure. The deuterium occupancy was refined to a value of 0.065(5), within error of the 0.07 occupancy expected for this site due to the complete filling of the oxygen vacancies with OD groups. Hence for the final refinement, the D occupancy was fixed to 0.07. The final refined structure has an approximate composition of SrZr_{0.86}Y_{0.14}O_{2.86}(OD)_{0.14}, which is consistent with the approximate amount of oxygen vacancies expected from X-ray and neutron diffraction of the dried sample. An illustration of the refined SrZr_{0.86}Y_{0.14}O_{2.86}(OD)_{0.14} structure is shown in Supplementary Fig. 25b, c, and the structural parameters in Supplementary Table 7. The O-D lengths refined to a value of 1.03(4) Å, consistent with expected O-H(D) lengths and with other reported O-H(D) containing perovskites^{54–56}. The presence of additional OH/OD bonds in the bulk perovskite confirmed by neutron diffraction explains that the considerable conductivity of the hydrated SZYO20 sample is indeed partly derived from the migration of protons and OH⁻ in the lattice.

Ab initio molecular dynamics simulations

To get a better understanding on the atomistic mechanism of proton and OH⁻ diffusion in SZYO20, we performed DFT based ab initio molecular dynamics (AIMD) simulations at 400 K. We started from a 2 × 2 × 3 supercell of SrZrO₃, which has a total of 72 × Sr atoms, 72 × Zr atoms and 216 × O atoms. We then created 8 oxygen vacancies, which are charge compensated by substitution of 16 × Zr⁴⁺ cations for 16 × Y³⁺ cations. This gives an effective chemical formula of SrZr_{0.78}Y_{0.22}O_{2.89}. Finally, we introduce 4 × H₂O molecules, which are split into 4 × OH⁻ and 4 × H⁺, with the 4 × OH⁻ each occupying an oxygen vacancy (after which only 4 oxygen vacancies remain in the cell), and the 4 × H⁺ each attaching to an O²⁻ anion. This leaves a total of 8 × OH⁻ (or 8 × H⁺) in the cell, and the AIMD simulations were performed for this cell. Due to the significant computational cost of running AIMD simulations for such a large cell, we were only able to run the AIMD simulations for a duration of 20 ps (a total of 40,000 MD time steps). Nevertheless, we were able to observe several interesting events, which include one local OH⁻ diffusion, several OH⁻ rotations, and multiple proton hopping. To illustrate the proton hopping during our AIMD simulations, in Fig. 6a, we show the distance between a selected proton and its neighbouring O atom (O6, as in the first frame of the production MD run) as a function of MD simulation time. For comparison, we show the distances between all the 8 protons and their neighbouring O atoms in the

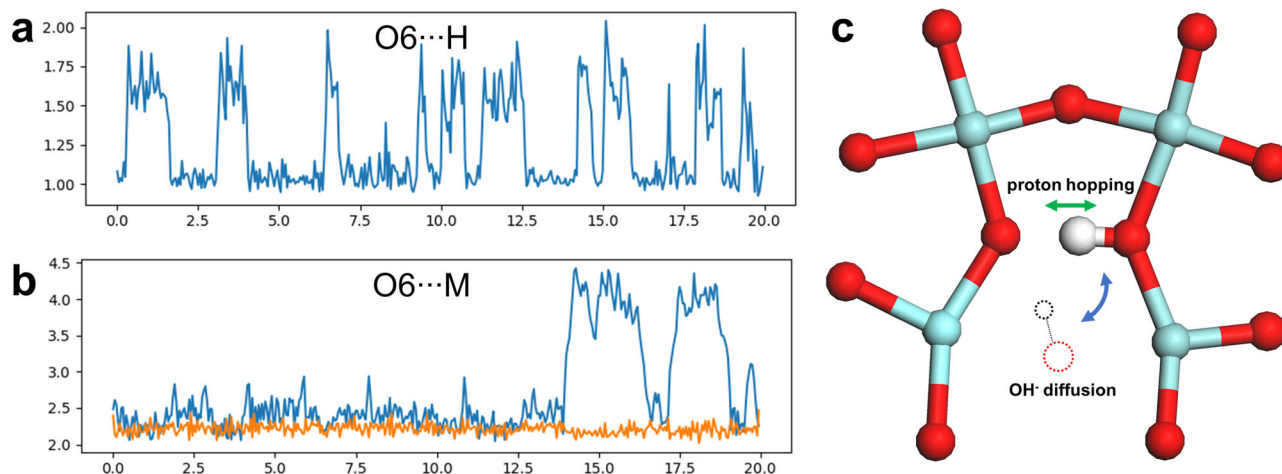


Fig. 6 | Molecular dynamics simulation of SZYO20. a Distance (in Å) between a selected proton and its neighbouring O atom as a function of MD simulation time (in ps). **b** Distance (in Å) between a selected oxygen atom (which was bonded to a proton initially) and its neighbouring B-site cations as a function of MD simulation time (in ps). The blue and orange lines represent the distances between an O^{2-} anion

and its two neighbouring B-site cations, respectively. **c** Schematic representation of possible atomistic mechanisms of proton hopping and OH^- diffusion. The dotted circles indicate new positions of OH^- after diffusion, with the previous site now becoming an oxygen vacancy. All other atoms are omitted for clarity. Colour code: red – oxygen, white – hydrogen, light green – zirconium or yttrium.

Supplementary Fig. 26. We find that apart from two protons (bonded to O1 and O7), most of the other protons hopped between neighbouring oxygen atoms, reflected by the changing $O \cdots H$ distances relative to the starting point of the MD simulation, and in a few cases, protons can hop back and forth, see e.g., the proton bonded to O6 (Fig. 6a). For the proton bonded to O4 initially, interestingly, it quickly hopped onto another nearby O^{2-} anion, which was followed by two separate OH^- rotations, and this proton did not come back to the original site within the 20 ps of AIMD simulation (reflected by the large $O \cdots H$ distance which is over 4 Å, see Supplementary Fig. 26). Similar OH^- rotations were also observed at the site of $O2 \cdots H$.

To obtain further insight, we also looked into the distances between the 8 oxygen atoms that were bonded to protons initially, and their neighbouring B-site cations, which can be either Zr^{4+} or Y^{3+} , and we show our results in Fig. 6b and Supplementary Fig. 27. As expected, majority of the O-metal distances show moderate oscillation behavior due to atomic vibrations at finite temperature (characterised by small and reversible changes in O-metal distances). However, the distance between O6 and one of the neighbouring B-site cations increased to ~4 Å at -15 ps and -18 ps (Fig. 6b), respectively, and we found this was related to OH^- diffusion. More specifically, the OH^- diffusion involves a OH^- ion exchanging position with a neighbouring oxygen vacancy as shown in the schematic in Fig. 6c. As can be seen, this process was stabilised by strong hydrogen bonding with another O^{2-} anion nearby, i.e. the strong hydrogen bonding is likely to reduce the transition barrier of this process in comparison with the diffusion of an individual O^{2-} anion. In combination with the OH^- rotations as observed in our AIMD simulations, this may help to explain the favourable OH^- conductivity observed in our experiment at a relatively low temperature of 90 °C.

With respect to the comparatively low proton conductivity at this temperature, we believe this is largely due to the orthorhombic crystal structure of SZYO20 at 90 °C, which leads to close oxygen–oxygen separations between the vertices of adjacent octahedra (Fig. 6c and Supplementary Table 8), and therefore protons are trapped between $O \cdots O$ (forming a very strong hydrogen bond)⁵⁷. At higher temperatures, $SrZrO_3$ goes through the $Pbnm$ to $I4/mcm$ phase transition, where the octahedral tilting becomes smaller, and the $O \cdots O$ distance between adjacent octahedra becomes smaller (Supplementary Table 8). This means the kinetic barrier of the rate-limiting step for proton diffusion, i.e., proton hopping from one side of the octahedron to

another (involving OH^- rotation), becomes smaller, and therefore the possibility that the proton gets trapped between $O \cdots O$ is much smaller, which may explain why proton conduction dominates at higher temperature in our experiment.

The OH^- ion diffusion involves the migration of OH^- ions to the neighbouring oxygen vacancies, the rotation of the OH^- ions in the vacancies, and the formation of strong hydrogen bonding with another neighbouring oxygen (Fig. 6c). Therefore, oxides with large cell volume, such as doped BZO, will facilitate the rotating of OH^- ions while those with small cell volume, such as doped CZO, will facilitate the diffusion of OH^- ions to the neighbouring oxygen vacancies and the formation of strong hydrogen bonding due to the short distance. Between BZO and CZO, an intermediate lattice, such as SZO, facilitates the rotation of OH^- ions, with a short distance for the diffusion of OH^- ions to the neighbouring oxygen vacancies and the formation of strong hydrogen bonding. This could be the reason why both pure and doped SZO exhibit the highest ionic conductivity in both $AZrO_3$ and $AZr_{0.8}Y_{0.2}O_{3-\delta}$ ($A = Ca, Sr, Ba$) series (Fig. 4a, Supplementary Fig. 13e).

Fuel cell feasibility study

After the discovery of a new ionic conductor, it is important to demonstrate its feasibility or potential in real applications. To further confirm the ionic conduction of SZYO20, a primary H_2 /air fuel cell and an NH_3 /air fuel cell using thick SZYO20 pellet as the electrolyte were fabricated (Supplementary Fig. 28). Figure 7a shows the OCV of the H_2 /air fuel cell at a temperature of 20 °C. The OCV gradually increased against time in the first three hours due to hydration then reached a stable value of 1.07 V. This is consistent with the conductivity measurements of unwashed SZYO20 in water at room temperature – although the initial conductivity is not high, over time the conductivity continues to increase until fully hydrated (Supplementary Fig. 6c). Therefore, pre-humidification is necessary in order to achieve high ionic conductivity and thus high OCV of a fuel cell. The observed OCV is fairly close to the theoretical value of a H_2/O_2 fuel cell (1.23 V at 25 °C) considering humidified air instead of pure O_2 was used at the cathode. From the observed OCV, it can be deduced that SZYO20 is a nearly pure ionic conductor at 20 °C in humidified atmosphere, which is consistent with the measured ionic transfer number (Fig. 4a). At 20 °C, a maximum current density of 1.25 mA cm^{-2} with maximum power density of 0.34 mW cm^{-2} was achieved respectively (Supplementary Fig. 29). The low power density is due to poor solid electrode/

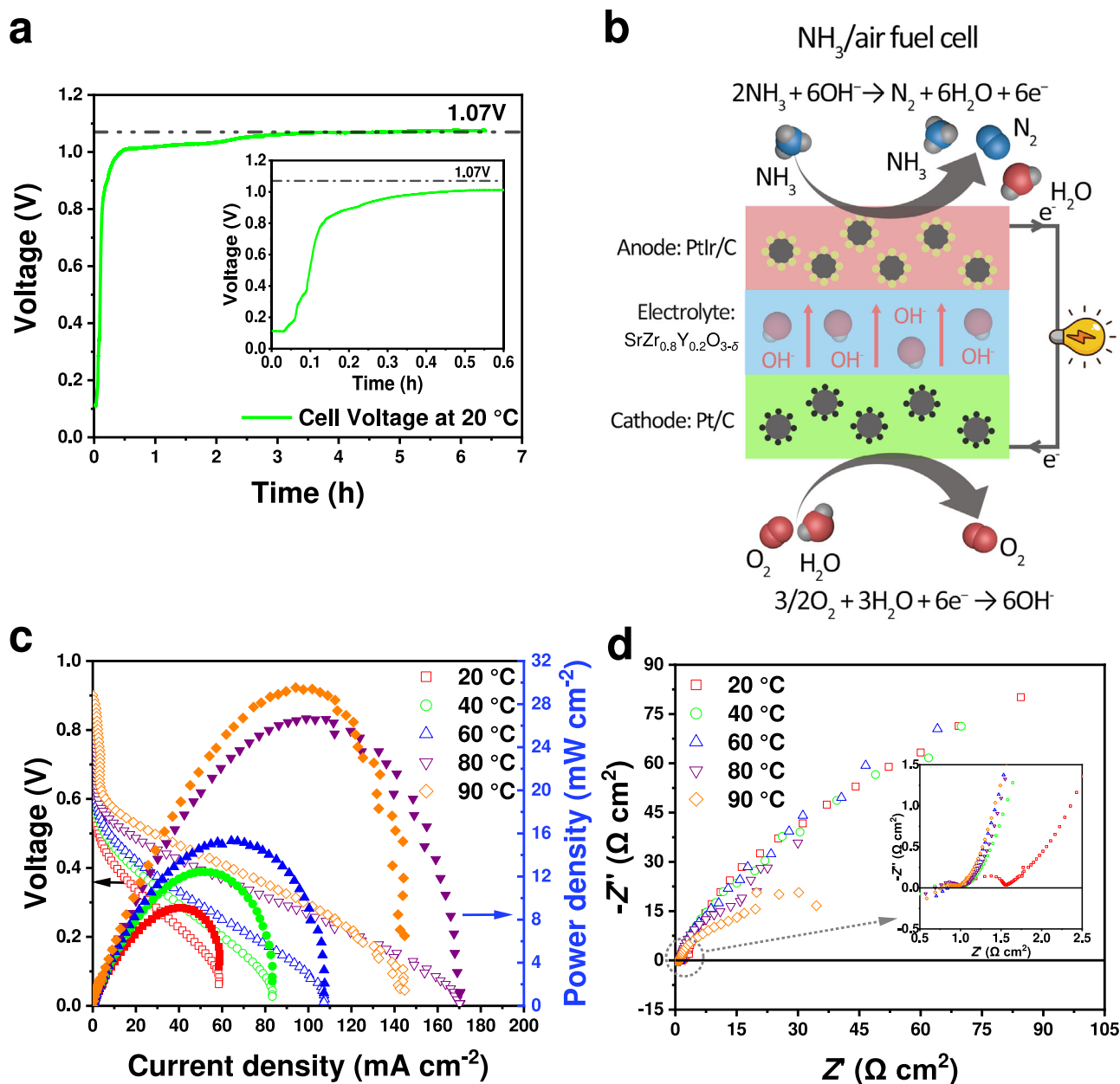


Fig. 7 | Fuel cell measurements when SZYO20 was used as electrolyte. a The OCV change against the time of a H₂/air fuel cell at 20 °C. **b** Working principle of low temperature SOFCs for an NH₃/air fuel cell. **c, d** The performance (c) and

impedance (d) of an NH₃/air fuel cell (35 wt% NH₃H₂O solution + 3 M KOH as the fuel) at different temperatures, enlarged impedance spectra are displayed in the insert.

electrolyte interfaces and unoptimized electrode microstructure. Although the power density is not attractive, compared to the state-of-the-art hydrogen fuel cells based on an acidic Nafion membrane, this key experiment indicates it is possible to develop NAT-SOFCs for different applications. The main purpose of this experiment was to confirm the OH⁻/H⁺ ionic conduction of SZYO20 electrolyte through OCV and fuel cell measurement thus the performance was not optimised. However, ceramic oxide mixed OH⁻/H⁺ conductor SZYO20 can work in neutral (water) or alkaline conditions, therefore potentially low-cost non-precious metal catalysts, such as perovskite oxides used in high temperature SOFCs, can be used as efficient electrocatalysts in both anode and cathode, which can dramatically reduce the overall cost of the fuel cell based on ceramic oxide electrolytes. In our recent study, it has been demonstrated that perovskite oxide LaCr_{0.25}Fe_{0.25}Co_{0.5}O_{3-δ} exhibits comparable activity for oxygen reduction reaction (ORR) to Pt/C cathode, demonstrated by comparable performance in direct

ammonia fuel cells (DAFCs) with a polymeric alkaline membrane electrolyte⁵⁸. Replacing the expensive acidic Nafion membrane in conventional PEMFCs with a mixed ceramic OH⁻/H⁺ conductor such as SZYO20 may significantly reduce the cost for both the electrolyte membrane and the electrode materials, and thus the cost of the whole fuel cell stack^{10,59}.

Ammonia fuel cells are important electrochemical devices to convert the carbon-free fuel ammonia to electricity at high efficiency^{60–63}. Potentially ammonia fuel cells can be used to power electric vehicles, bypassing the problems of storage and transport of hydrogen^{60,64}. The ceramic oxide ionic conducting electrolyte can be fully humidified if a liquid fuel such as ammonia solution is used at the anode. Therefore, the ceramic oxide SZYO20 is particularly suitable to be used as electrolyte for fuel cells using liquid fuels when the anode side is exposed to water, or electrolyzers for splitting liquid water into hydrogen when both anode and cathode sides are exposed to water.

Here, ammonia was also tested as the fuel for this type of NAT-SOFC based on a thick SZYO20 electrolyte (Fig. 7b). When 35 wt% ammonia solution was used as the fuel, the current density of the fuel cell electrolyte was comparable to the fuel cell using commercial anion exchange membrane (AEM) (Supplementary Figs. 30, 31). The DAFC retained a relatively good durability for over 20 h when using pure ammonia solution as a fuel (Supplementary Fig. 30c) indicating good chemical compatibility of SZYO20 with CO₂ in air at the cathode. The oscillation of the measured voltage is due to the unstable cell temperature from the home-made testing jig using heating cartridges to provide the required temperature.

Considering the thickness difference between SZYO20 pellet (1300 μm) and AEM (50 μm), the conductivity of SZYO20 pellet, is estimated from the series resistance of the a.c. impedance spectra of the fuel cells, are higher than the commercial AEM (Supplementary Fig. 32). The observed low ionic conductivity of commercial AEM is due to its poor chemical compatibility with CO₂ in air, which was used as the oxidant at the cathode. It has been reported that adding KOH in ammonia solution can significantly improve the fuel cell performance when an alkaline membrane was used as the electrolyte^{62,63}. Further tests were performed with a 35 wt% ammonia solution, with added 3 M KOH as the fuel for a DAFC based on SZYO20 electrolyte. The relevant I-V curves and a.c. impedance spectra of this DAFC are shown in Fig. 7c, d. At 90 °C, a maximum power density of 30 mW cm⁻² was achieved, which is comparable to the power density of an NH₃/air fuel cell at 80 °C, based on commercial polymeric alkaline membrane electrolyte and CO₂-free air⁵⁸. It should be noted that the ammonia fuel cell in this study was measured under ambient pressure with compressed air with CO₂ while the ammonia fuel cells in the previous study were carried out under an applied back-pressure⁵⁸. The mechanical strength of the SZYO20 pellet is not high, thus the ammonia fuel cell measurement was not carried out under pressure. The mechanical strength of oxide materials can be tailored/improved by doping strategy. Considering the thickness difference of the electrolyte, 1300 μm of the oxide electrolyte SZYO20 vs. 50 μm of the commercial polymeric AEM electrolyte, there is a huge potential to further improve the power density of the DAFCs when thin-film technology used in conventional SOFCs or solid-state lithium-ion batteries, such as tape-casting, laser deposition, are used in the preparation of the NAT-SOFCs⁴⁰. In conclusion, good ionic conduction of SZYO20 at NAT has been demonstrated in both hydrogen and ammonia fuel cells. The aim of the fuel cell study is to demonstrate the feasibility in real applications while the power density can be greatly improved through the reduction of the thickness of the electrolyte, improvement in the solid electrolyte/electrode interfaces, optimisation of the microstructure of the electrode to achieve a level for real applications. The high ionic conductivity of the ceramic oxide electrolyte at a temperature below 100 °C and the excellent chemical stability and compatibility with CO₂ in air, have overcome the key problems associated to conventional AFCs and AMFCs. Similar to conventional PEMFCs based on acidic Nafion membrane, humidifying the fuels and air is necessary in order to maintain high ionic conductivity of the electrolyte unless liquid fuels such as ammonia/methanol/ethanol solution is used at the anode or/and liquid oxidant such as H₂O₂ solution is used at the cathode⁶⁵.

Conductivity measurements using fuel cell testing jig

As shown in Supplementary Table 4, some of the perovskite may partially dissolve in water over time, leading to increased liquid water conductivity. The liquid conductivity due to additional dissolved species could result in a slightly higher measured conductivity compared to the real conductivity when using the testing jig shown in Supplementary Fig. 5. To avoid the influence of the ionic conductivity of surrounding water or solution, the fuel cell testing jig shown in Supplementary Fig. 33 was used to measure the conductivity of SZYO20 and CZYO20 pellets. When the fuel cell testing jig was used, it

is inevitable that some ions will transfer outside the silver electrodes (1 cm²), contributing to the measured conductivity, thus it is also difficult to obtain a completely accurate conductivity value from our fuel cell setup. Therefore, we calculate the conductivity in two areas, the area of the whole pellet (dot lines in Supplementary Figs. 34, 35) and the area covered by silver electrode. The real conductivity should be between these two values. For SZYO20, the conductivity measured by the conventional conductivity testing jig (Supplementary Fig. 5) is between the two values calculated using the different pellet areas (Supplementary Fig. 34a, b), which supports the conductivity as measured by the original jig as reliable. When comparing the conductivity of SZYO20 sintered at 1300 °C and 1500 °C respectively, in water, the conductivity of the 1500 °C sintered pellet is slightly lower than that sintered at 1300 °C (Supplementary Fig. 34c), which implies that the conductivity is not only related to the bulk, but also to the surface of the pellet. The relative density of SZYO20 is 94% when sintered at 1500 °C, which is higher than 80% when sintered at 1300 °C (Supplementary Table 9 and Supplementary Note 4). Ions particularly protons may diffuse along the grain boundary together with water molecules via a vehicle mechanism, similar to that in Nafion membrane, causing high H⁺ ionic conduction. Additionally, surface protonic conductivity in wet atmospheres has been reported on porous oxides including monoclinic ZrO₂⁶⁶ and porous nanoscopic CeO₂⁶⁷, which may partially explain the ionic conductivity of some relatively low relative-density materials investigated in our work. A similar phenomenon was also observed for 1300 °C and 1500 °C sintered CZYO20 pellets while the sample sintered at higher temperatures with higher density exhibited relatively lower conductivity (Supplementary Fig. 35a). For dense CZYO20 pellet sintered at 1500 °C, the measured conductivity in water using the fuel cell testing jig calculated from the electrode coverage area (1 cm²) is comparable to that measured in the conventional conductivity measurement jig (Supplementary Fig. 35b).

Conductivity of dense CZYO20 pellets in KOH solutions

The key advantage of the conductivity measurement using the fuel cell type testing jig is, it can remove the effects of ionic conductivity of surrounding solution such as water or any other solutions. In our study of DAFCs, it was found that the normalised series resistance of the fuel cell is only 1.1 Ω cm² when 35 wt% NH₃H₂O solution + 3 M KOH was used as the fuel (Fig. 7d) when the operating temperature is above 40 °C. This corresponds to an ionic conductivity of 0.11 S cm⁻¹ considering a thick pellet electrolyte was used. It is likely that the added KOH will increase the ionic conductivity of the SZYO20 pellet. Considering the relative density of the 1300 °C SZYO20 pellet used in the DAFC measurements was only 80%, KOH may also diffuse into the holes of the pellet, leading to increased OH⁻ ionic conductivity, similar to the case of alkaline membrane fuel cells based on polymeric alkaline membranes. To eliminate the effects of holes, we tested the ionic conductivity of dense CZYO20 pellets sintered at 1500 °C with a relative density of 99% (Supplementary Table 9) in water, 1 M, 3 M and 6 M KOH solutions, using the fuel cell testing jig. As shown in Supplementary Fig. 35c, the ionic conductivity continued to increase with increased KOH concentration. At 90 °C, when the dense CZYO20 is exposed in 6 M KOH solution, its conductivity is approximately 0.1 S cm⁻¹, comparable to that of Nafion membrane. This is also 100 times higher than the ionic conductivity of CZYO20 in pure water at 90 °C (Supplementary Fig. 35b). At 25 °C, the conductivity is still as high as 4.8 × 10⁻² S cm⁻¹, which is high enough to be used as an electrolyte for fuel cells and electrolyzers. We also tested the ionic conductivity of dense CZO pellets sintered at 1500 °C (dash lines in Supplementary Fig. 35d), which was one-fifth of that of dense CZYO20 in 1 M KOH and half of that in 6 M KOH. This further confirms that oxygen vacancies in the lattice produced from doping still play a critical role in high ionic conductivity of dense pellets even when the concentration of charge carriers, OH⁻, is quite high in the surrounding

environment. These dense oxide materials can be used as the electrolyte in alkaline or alkaline membrane electrolyzers while both sides of the separating membrane are soaked in concentrated aqueous alkaline solution. This kind of electrolyser based on solid oxide electrolyte such as CZYO20 can be called near ambient solid oxide electrolytic cells (NAT-SOECs).

Electrolysis of H₂¹⁸O and D₂O using dense CZYO20 as the electrolyte

In order to have a better understanding of the key role of OH⁻ ionic conduction of the perovskite oxides, we carried out electrolysis experiments in 20% H₂¹⁸O, pure D₂O, and 1 M KOH dissolved in D₂O when dense CZYO20 was used as the electrolyte. Following the electrolysis experiments, Raman spectroscopy was used to detect the ¹⁸O labelled water, while Fourier-transform infrared spectroscopy (FTIR) was used to detect the H₂O, HDO and D₂O species in solutions (Supplementary Figs. 36–38 and Supplementary Note 5).

One side of the electrolytic cell, for hydrogen evolution reaction (HER), was circulated with 20% H₂¹⁸O in H₂¹⁶O, the other side, for oxygen evolution reaction (OER), was circulated with pure H₂¹⁶O. It has been reported that an extra band at 684 cm⁻¹ was observed for ¹⁸O-labelled NaOCl in Raman spectroscopy, along with the O-Cl stretching band of NaOCl observed at 711 cm⁻¹⁶⁸. Therefore, the NaOCl solution was used as an additive to detect the presence of H₂¹⁸O and ¹⁸OH⁻ species during electrolysis. The transfer of oxygen (¹⁸O) from the HER side to the OER side after applying 2 V constant voltage through the electrolytic cell for a certain time was confirmed by the observed 683 cm⁻¹ Raman spectra in Supplementary Fig 36c–e, while no ¹⁸O labelled species were detected on the OER side when there was no potential applied (green line in Supplementary Fig. 36e). This indicates the H₂¹⁸O did not spontaneously diffuse through the dense CZYO20 pellet without any potential applied, and the conduction of ¹⁸O labelling species (e.g., ¹⁸OH⁻) through the pellet has been verified.

Similarly, pure D₂O was circulated in the HER side of the electrolyser for D₂ evolution reaction. When there is no potential applied for 43 h, no D₂O was detected on the other side, indicating that D₂O itself cannot automatically diffuse through the dense CZYO20 pellet, as expected (blue line in Supplementary Fig. 37b). However, after applying 2 V constant voltage through the cell for 100 h, the HDO peaks at absorbance bands of 1450 cm⁻¹ and 2504 cm⁻¹⁷⁰ in FTIR spectra were observed in pure H₂O on other side, indicating the material conducting OH⁻ or OD⁻ ions. Along with the confirmation of oxygen exchange in the electrolysis of H₂¹⁸O, the OH⁻ ionic conduction of dense CZYO20 is further demonstrated by the D₂O electrolysis experiments. It was found the HDO signal became stronger with extended duration of electrolysis (Supplementary Fig. 37c). Weak D₂O signal, the absorbance band at 1200 cm⁻¹⁶⁹, was found when the duration of applied 2 V was over 35 h, indicating D₂O can diffuse across the dense pellet under certain applied DC voltage for a long time. The diffusion of smaller H₂O is expected to be easier thus dense CZYO20 can be potentially used for water separation when a DC voltage (or current) is applied through the cell. This has potential applications in seawater desalination or wastewater treatment.

In the experiments of electrolysis of both H₂¹⁸O and D₂O respectively, under applied DC voltage, both ¹⁸O and D can transport through the dense CZYO20 pellets in water, which indicates most likely the labelled ¹⁸O and D isotopes are transferred through the OH⁻ ions.

To further investigate the OH⁻ ionic conduction, 1 M KOH dissolved in D₂O was used in the HER catalytic side of the electrolytic cell. In order to investigate the crossover of KOH through the dense electrolyte pellet, CO₂ gas was purged into the solution of OER side after electrolysis. If there are KOH species in the solution, the 1370 cm⁻¹ peak assigned to K₂CO₃ should be observed in FTIR spectra when CO₂ is present⁷⁰. From the blue line in Supplementary Fig. 38c, no HDO/D₂O peaks were observed when one side of the cell was exposed to 1 M

KOH-D₂O solution indicating no D₂O can diffuse through the dense CZYO20 pellet, the same as the case for pure D₂O. When 2 V DC voltage was applied through the cell for 16 h, the signal of HDO was observed in pure water on the other side. However, no K₂CO₃ and thus no KOH was observed, indicating OD⁻ ions diffused from the KOH-D₂O side to the H₂O side while KOH molecules did not (Supplementary Fig. 38d). This experiment indicates the OD⁻ ions were transferred through the oxide materials. When 1 M KOH was used, the OH⁻ concentration was much higher than that in pure H₂O which relies on the self-dissociation of H₂O,



The concentration of OH⁻ ions from self-dissociated H₂O (Eq. 3) is very low, about 10⁻⁷ M at 25 °C. When the dense CZYO20 was exposed to 1 M KOH-D₂O solution, the concentration of OH⁻ ions from KOH was about 1 M, about 7 orders of magnitude higher than that of pure H₂O. The OH⁻ ions from KOH therefore act as ‘feeding ions’, i.e., when in contact with the nearest oxygen vacancies, these ions can diffuse through the lattice, leading to very high OH⁻ ionic conduction. This has the effect of suddenly increasing the concentration of mobile ions. This also explains why the conductivity of CZYO20 in 6 M KOH is 100 times higher than that in pure H₂O. As the pellet is very dense, it is reasonable to speculate that the high OH⁻ ionic conductivity is also related to the bulk material, i.e., OH⁻ ions are also transferred through the oxide lattice.

The SEM images of the cross-section of the dense CZYO20 pellet before and after the conductivity in water and KOH solution are shown in Supplementary Figs. 39, 40 respectively. Element mapping indicates there is a weak K signal along the cross-section after the conductivity measurement. This suggests that K⁺ ion can also diffuse into the grain boundary of the CZYO20 pellet. No K₂CO₃ was observed on the pure H₂O side in the electrolysis of 1 M KOH-D₂O solution, because the direction of applied voltage only allows negatively charged OH⁻ or OD⁻ ions to diffuse to the waterside while the positively charged K⁺ ions should diffuse to the opposite direction, the D₂O side. The presence of KOH in the cross-section of dense CZYO20 pellets after the conductivity measurements in KOH, indicates KOH can also diffuse into the grain boundary of the oxide, which may form another pathway for OH⁻ ions, leading to the high ionic conductivity.

From the analyses above, OH⁻ ions may transfer through both the oxide lattice and the grain boundary where KOH has been diffused. Both may make contributions to the high OH⁻ ionic conductivity of CZYO20 in concentrated KOH solution. However, the ionic conductivity of doped CZYO20 with extrinsic oxygen vacancies is much higher than that of pure CZO with limited intrinsic oxygen vacancies in both 1 M and 6 M KOH aqueous indicating the oxygen vacancies in the oxide lattice play a crucial role for the higher ionic conductivity in perovskite oxides (Supplementary Fig. 35d).

From solid-state NMR measurements, the hydrogen or hydrogen-related species such as OH⁻ ions in CZYO20 is also associated with Y³⁺ ions, where the oxygen vacancies are in the vicinity of Y³⁺ ions, thus it is believed the H⁺ and/or OH⁻ ions are associated to oxygen vacancies (Supplementary Fig. 21). This is the same as that for SZYO20. It is therefore reasonably deduced that both SZYO20 and CZYO20 share the same ionic conduction mechanism.

Discussion

In summary, the mixed OH⁻/H⁺ conduction of perovskite oxides such as SZYO20 and CZYO20 with high ionic conductivity in water and humidified air was discovered. Concentration cell measurements indicate about 70% of the charge carriers in fully-hydrated SZYO20 at room temperature are OH⁻ ions which means it is mainly an OH⁻ ionic conductor. This is very different from the known proton conduction in doped zirconates at high temperatures, typically above 500 °C. XRD

and ADF-STEM have confirmed the formation and excellent stability of the perovskite phase SZYO2O. Neutron diffraction and XRD refinement show that there are oxygen vacancies in unhydrated SZYO2O (with $\delta = 0.07$). This ceramic oxide OH^-/H^+ ionic conductor exhibits excellent chemical stability in water/steam and CO_2 in air, overcoming key problems of the electrolytes in conventional AFCs and AMFCs. Equivalent electrochemical circuit simulation on EIS has extracted the bulk and grain boundary conductivity of samples, which suggests, that for SZYO2O, the conductive ions not only diffuse in the perovskite lattice but may also transport through the grain boundaries. After being fully hydrated, the presence of hydrogen and additional oxygen atoms in the SZYO2O bulk has been verified by neutron diffraction analysis. A combination of intra-proton transfer and OH^- migration within the lattice could be taking place resulting in the observed high conductivity.

Solid state NMR study reveals that the exchange between OH^- and H^+ ions in partially hydrated SZYO2O and, transfer of OH^- and H^+ ions is coupled with dopant Y^{3+} ions at the B-sites indicating oxygen vacancies play an important role for the ionic conduction. This is consistent with the DFT calculations, which showed that the migration of OH^- ions in SZYO2O relies on the diffusion of OH^- ions to the neighboring oxygen vacancies, which then rotate at a right angle to form a strong hydrogen bond with the closest oxygen. The high ionic conductivity of these perovskite oxides requires the presence of liquid water to facilitate hydrogen bonding and the corresponding OH^- ion migration. In situ high-temperature NMR and Raman spectra have further confirmed the loss of hydrogen bonds and mobile OH^- in hydrated oxide at high temperatures, consistent with the measured conductivity data against temperature. Thick SZYO2O pellets (1.8 mm and 1.3 mm for H_2/air and NH_3/air fuel cells respectively) were used to make fuel cells and the feasibility of the ceramic mixed OH^-/H^+ ionic conductor in fuel cell application has been demonstrated.

It was found denser SZYO2O and CZYO2O pellets exhibit relatively lower ionic conductivity in pure water. This indicates the ionic conduction is not only the bulk but could also be the surface conduction through the grain boundary. Protons might also diffuse through the grain boundary via a vehicle mechanism, similar to H_3O^+ ions in polymeric Nafion membrane.

Slowly dissolution of perovskite oxides in water has been observed through conductivity and pH measurements, while the contribution of the dissolved species from the perovskite to the measured high ionic conductivity of the oxides is negligible. To eliminate the effects of dissolved species from the perovskite in water on the measured conductivity, a fuel cell testing jig was used in the conductivity measurement of both SZYO2O and CZYO2O. The measured conductivity from a conventional conductivity measuring jig and the fuel cell testing jig is comparable. The conductivity of dense CZYO2O and CZO pellets in concentrated KOH aqueous solution was also measured by the fuel cell testing jig. It was found that the ionic conductivity of dense CZYO2O in 6 M KOH is approximately 0.15 cm^{-1} at 90°C , which is 100 times that in pure water. This shows that when a ceramic material is submerged in a concentrated KOH solution, the ionic conductivity can be significantly increased. Compared to CZO, much higher ionic conductivity was observed in doped CZYO2O indicating oxygen vacancies in the oxide lattice greatly facilitate the transfer of ions, such as OH^- ions. Through the experiments of electrolysis of H_2^{18}O , D_2O and 1 M KOH- D_2O , as well as the EDX element analysis of dense CZYO2O after conductivity measurement in KOH, the possible pathways of OH^- ions could be both the oxide lattice and KOH diffused into the grain boundary of oxide pellets. The phenomenon of ionic conductivity of CZYO2O significantly enhanced in KOH solution suggests the possibility that trace amounts of residual $\text{Sr}(\text{OH})_2$ and/or $\text{Y}(\text{OH})_3$ from hydrolysis of SrY_2O_4 in a sample with nominal composition of SZYO2O may similarly provide some OH^- feed ions or O-H

transport channels, facilitating the OH^- ion transfer resulting in high ionic conductivity.

Perovskite oxides have been reported as excellent electrochemical catalysts for both high-temperature solid oxide fuel cells and low-temperature electrochemical devices such as fuel cells and electrolyzers^{2,58,59,71,72}. If some multi-valence transition elements are introduced into the B-sites of SZYO2O, mixed ionic-electronic conductors may be formed which could be potential electrocatalysts for electrochemical devices.

The discovery of low-temperature mixed OH^-/H^+ ionic conduction in oxide materials such as SZYO2O opens a window to discovering new low-temperature OH^-/H^+ ionic conducting materials in oxides or other ceramic materials. Adding KOH to the fuel of DAFCs significantly increased the OH^- ionic conductivity, which has been further demonstrated with conductivity measurements in concentrated KOH and electrolysis of H_2^{18}O and D_2O using a dense CZYO2O pellet as the electrolyte. The significantly increased ionic conductivity of both CZYO2O and CZO in KOH solutions will provide a new route to develop new ionic conducting materials for electrochemical devices, such as electrolyzers, fuel cells and batteries. A similar phenomenon has also been observed in other oxides such as doped cerates in our lab, while the investigation remains ongoing. For practical application of these oxide ionic conducting materials in electrochemical devices, the matched electrode materials and the electrode/electrolyte interface, etc. must show good performance and be compatible which requires further investigation.

Methods

Synthesis of $\text{AZr}_{1-x}\text{Y}_x\text{O}_{3-\delta}$ ($\text{A} = \text{Ca, Sr, Ba, } x = 0, 0.1, 0.2$)

The perovskite oxides $\text{SrZr}_{0.8}\text{Y}_{0.2}\text{O}_{3-\delta}$ (SZYO2O) were synthesized by a combustion method. 10.80 g of $\text{Sr}(\text{NO}_3)_2$ (98%, Alfa Aesar), 3.83 g of $\text{Y}(\text{NO}_3)_3 \cdot 6\text{H}_2\text{O}$ (99.9%, Alfa Aesar), 13.15 g of $\text{ZrOCl}_2 \cdot 8\text{H}_2\text{O}$ (98%, Alfa Aesar) and 5 mL of nitric acid (70%, Sigma Aldrich) were directly dissolved in deionized water to prepare a mixed solution. Then 38.81 g of citric acid (99 + %, Alfa Aesar) was added into the solution and magnetically stirred at 90°C for 12 h on a hot plate to form a gel. Then the gel was dried at a constant temperature of 400°C for 1 h to be ignited for combustion. After the organic components in the mixture burned off, the powder was ground in an agate mortar and calcined in air at 400°C for 3 h, then 1000°C for 2 h. After this, the as-prepared powder was reground and pressed into pellets with a diameter of 13 mm and 20 mm respectively under a pressure of 6 tons, and then sintered in air at 1300°C for 24 h with a heating/cooling rate of 5°C min^{-1} to form SZYO2O phase⁷³. Pellets were also sintered at 1500°C to get higher relative density.

The perovskite oxides SrZrO_3 (SZO) and $\text{SrZr}_{0.9}\text{Y}_{0.1}\text{O}_{3-\delta}$ (SZYO1O) were synthesized with the same combustion method. $\text{Sr}(\text{NO}_3)_2$, $\text{Y}(\text{NO}_3)_3 \cdot 6\text{H}_2\text{O}$ and $\text{ZrOCl}_2 \cdot 8\text{H}_2\text{O}$ according to the corresponding stoichiometric molar ratio with a small amount of nitric acid were used in precursor solution. The molar ratio of citric acid to total metal ions was 2:1⁷⁴. The target perovskite phase was obtained after pelletized and fired at 1300°C , the same as for preparation of SZYO2O.

The perovskite oxides CaZrO_3 (CZO), $\text{CaZr}_{0.8}\text{Y}_{0.2}\text{O}_{3-\delta}$ (CZYO2O), BaZrO_3 (BZO) and $\text{BaZr}_{0.8}\text{Y}_{0.2}\text{O}_{3-\delta}$ (BZYO2O) were synthesized by the same combustion process. 16.70 g of $\text{Ca}(\text{NO}_3)_2 \cdot 4\text{H}_2\text{O}$ (99%, Sigma Aldrich) or 13.20 g of $\text{Ba}(\text{NO}_3)_2$ (99%, Sigma Aldrich) was used as precursors respectively to synthesize AZrO_3 and $\text{AZr}_{0.8}\text{Y}_{0.2}\text{O}_{3-\delta}$ ($\text{A} = \text{Ca, Ba}$). The usage of other precursors and igniting conditions were the same as for SZO and SZYO2O. The CZO and CZYO2O pellets were sintered at 1300°C or 1500°C while the BZO and BZYO2O pellets were sintered at 1500°C .

The relative densities of the pellets are detailed in Supplementary Note 4 and Supplementary Table 9.

The as-prepared pellets with a diameter of about 13 mm were used for conductivity measurements while those with a diameter of about

20 mm were used for concentration cell and fuel cell jig measurements.

Synthesis of SrY₂O₄ and Y(OH)₃

In order to identify the effect of the secondary phase SrY₂O₄ in SZYO20 on the ionic conductivity, the single phase SrY₂O₄ was synthesised by the same combustion method. 6.48 g of Sr(NO₃)₂, 23.00 g of Y(NO₃)₃ · 6H₂O and 34.93 g of citric acid were directly dissolved in deionized water and the mixed solution was magnetically stirred at 80 °C for 12 h on a hot plate to form a gel. The igniting conditions were the same as for SZYO20. The target SrY₂O₄ sample was obtained after pelletized and fired in air at 1300 °C for 24 h.

In order to rule out the contribution of the hydrolysis products of SrY₂O₄ on the conductivity measurement, Y(OH)₃ sample was chemically deposited through the reaction between 0.5 mol L⁻¹ Y(NO₃)₃ · 6H₂O and 1.5 mol L⁻¹ of NaOH (98%, Alfa Aesar). The synthesized powder was thoroughly washed and dried at 60 °C for 8 h, and then pelletized for conductivity measurement. The commercial Y₂O₃ (99.9%, Alfa Aesar) powder was also pelletized and fired at 1300 °C for 4 h to measure its conductivity in water. (Supplementary Fig. 7)

Structural characterizations

The X-ray diffraction (XRD) was carried out on a third-generation Malvern Panalytical Empyrean equipped with multicore (iCore/dCore) optics and a Pixcel3D detector operating in 1D scanning mode with a Cu K α radiation (1.5419 Å) to identify the crystalline phases present in the samples. The diffraction scans were collected over a 2 θ range from 5° to 100° at a step size of 0.013° with a counting time of 110 s per step and were analyzed using the Malvern Panalytical Highscore Plus 4.9 software and the latest ICDD PDF-4+ database. The 2 θ scan range was widened to 5–140° along the diffraction scanning time extended to 4 or 15 h to obtain high-quality XRD data for refinement. Rietveld refinement of the representative perovskite oxides was carried out by GSAS-II⁷⁵. The crystallographic refinement parameters are listed in Supplementary Table 1.

Scanning electron microscopy (SEM) observation of the microstructure was carried out on a Zeiss SUPRA 55-VP scanning microscope. Energy dispersive X-ray spectroscopy (EDX) was used to analyze the cross-section of pellets and determine the element composition of the samples through elemental mapping analyses.

Annular dark field (ADF) and bright field (BF) scanning transmission electron microscopy (STEM) imaging and EDX elemental mapping were carried out on a double aberration-corrected JEOL ARM200F TEM, operated at 200 kV, equipped with a 100 mm² Oxford Instruments windowless EDX detector. The SZYO20 powders for TEM measurement were ground from sintered pellets. Some pellets were washed in water at 90 °C three times to get rid of the second phase SrY₂O₄ and hydrated products and then ground into powders, labelled as washed SZYO20 samples. It is noted that Cu, Cr and C signals are artefacts generated during the STEM-EDX acquisition.

Raman spectra at room temperature were recorded on a Renishaw inVia Reflex Raman Microscope equipped with DPSS laser at 532 nm (10% power nominally 2 mW) and Renishaw CCD detector. Objective of X50 LWD and an acquisition time of 10 s was used during testing. For these measurements, the pellets were cleaved, and the fracture surface was analysed. The sample washed in water at 90 °C and dried in an oven for overnight was labeled as partially hydrated sample, while the sample dried in air for a moment before Raman measurement was labelled as hydrated sample. High-temperature Raman spectra of hydrated sample powders were recorded from room temperature to 1000 °C. Measurements were performed during the heating process, using the same instrumentation and conditions. The samples were mounted in a temperature-controlled heating stage, which was placed under the objective lens of the microscope for the high-temperature measurements. It adopted an average heating rate

of 20 °C min⁻¹. Raman spectra of ¹⁶O and ¹⁸O labelled liquid samples were obtained at 514.5 nm laser (100% power nominally 26 mW) with an 1800 l/mm grating and an acquisition time of 20 s × 10 accumulation. Liquid samples were put in a Helma Quartz Cuvette and mounted in a Cuvette holder accessory for measurement.

Simultaneous Thermal Analysis (STA) was carried out by a TA Instruments SDT 650 operating under an air atmosphere at 50 ml min⁻¹. The sample was loaded into a pre-tared 90 μ l alumina pan. The analysis was performed from 25 to 1000 °C at a constant heating rate of 10 °C min⁻¹.

Fourier-transform infrared spectra (FTIR) of D₂O and H₂O liquid droplets were acquired using a Jasco FTIR-4200 (Type A) spectrometer equipped with a MIRacle Single Reflection ATR accessory with Diamond/ZnSe crystal (Pike Technologies). Measurements were collected between 4000 and 400 cm⁻¹ at a resolution of 2 cm⁻¹ with 100 scans per sample. Standard High-intensity ceramic source and a triglycine sulphate (TGS) detector were used. In order to remove atmospheric CO₂ and H₂O peaks from sample measurements, background spectra and sample spectra were collected while continuous purging the instrument with N₂.

Solid-State NMR spectra measurements

All SZYO20 powder samples for solid state nuclear magnetic resonance (NMR) measurements were heated in hot water at 90 °C for 20 h and washed to get rid of second phase SrY₂O₄ and the hydrated products. This process was repeated three times for each sample. The as-treated powder was dried in a fume cupboard at room temperature overnight, labelled as partially hydrated sample. Some of the as-treated powder was dried in a vacuum oven at 120 °C overnight to get rid of the hydrated water. This sample was labelled as dry SZYO20 sample.

CZY020 powder samples for solid state NMR measurements were pre-treated through the same process as SZYO20 sample, labelled as water-hydrated CZYO20 and dry CZYO20 respectively. The sample after conductivity measurement in KOH solution was labelled as KOH-hydrated CZYO20.

NMR were performed on a Bruker Avance Neo spectrometer with a Larmor frequency of 850.2 MHz and 41.6 MHz for ¹H and ⁸⁹Y, respectively using a 1.3 mm Bruker triple resonance HXY probe spinning at 60 kHz and a 4 mm Bruker double resonance HX low gamma probe spinning at 8 kHz. The ⁸⁹Y spectra were referenced to solid Y(NO₃)₃ · 6H₂O with the ⁸⁹Y peak set to -53.2 ppm. The ¹H NMR spectra were referenced to ¹H peak of solid adamantane set to 1.8 ppm. ⁸⁹Y MAS spectra were acquired with a spin echo pulse sequence with a 90 and 180 pulses set to 6 μ s and 12 μ s, respectively and with cross polarisation experiment with 6 ms contact time. ¹H MAS (60 kHz) NMR spectra were measured using a background suppression pulse sequence consisting of a 180 pulse followed by two 90 pulses. ¹H MAS spectra at 25, 95 and 125 °C on partially hydrated SZYO20 were recorded with a 1.6 mm HXY Phoenix NMR probe spinning at 30 kHz.

Neutron diffraction measurements

SZYO20 powders dried in a vacuum oven at 180 °C for 40 h were labelled as vacuum-dried SZYO20. Some of the powders were pre-washed in hot water at 90 °C for 20 h for three times to get rid of the second phase SrY₂O₄ and the hydrated products. Then the washed powders were heated with an excess amount of D₂O liquid in a hydrothermal bomb at 225 °C for 12 h, labelled as deuterated SZYO20.

Neutron powder diffraction (NPD) patterns were collected at room temperature on the time-of-flight high-resolution powder diffractometer (HRPD) at ISIS⁷⁶. Data were collected for vacuum-dried and deuterated samples of SZYO20. The samples were loaded into thin-walled (150 μ m) cylindrical vanadium foil sample holders with 7.94 mm diameter. The sample holders were mounted on the rotary sample changer and maintained under the sample vacuum tank (-0.15 mbar)

for the duration of the measurements. Full intensity profiles were recorded with all three detector banks: bank 1 the highest resolution backscattering bank, bank 2 the 90-degree detectors and bank 3 the low-resolution forward scattering array. Samples were each measured for several hours. Data were normalised to the incident spectrum and corrected for instrument efficiency using a V:Nb null scattering standard, and then corrected for sample attenuation using the software Mantis⁷⁷. The attenuation was calculated from the total scattering cross section, the absorption cross-section and the number density of each sample based on its chemical stoichiometry, volume and mass. As the exact amount of D₂O in the deuterated samples was not known at the time, their scattering and absorption cross-sections were calculated on the basis of the anhydrous chemical composition. Since the concentration of D₂O in the structure proved to be very small, its contribution to the attenuation will be negligible. The collected NPD patterns were refined using the Rietveld method with the GSAS-II software⁷⁵. Only data from bank 1 was used for refinement. Details of the refinement, including the process by which the deuterium atoms were located, are given in the Supplementary Note 3.

Measurements of ion conductivity and ion transfer number

To measure the conductivity of sintered oxide pellets with a diameter around 13 mm, two side surfaces of a pellet (~2 mm in thickness) are coated by Silver Conductive Ink (Alfa Aesar) to form Ag electrodes. The Ag painting layers were dried in an oven at 130 °C for 150 min. A sandwich-structure cell with a layer of pellet between two layers of silver mesh was then immobilized in a home-made jig. Since the conduction of hydroxide ions requires water or steam as a medium, the ionic conductivity was measured either in a beaker fulfilled with deionized water (Supplementary Fig. 5) or in a sealed quartz tube in which the humidified compressed air was passing through. For the conductivity measurements in water, the temperature of water was detected and controlled by a hot plate connected with thermocouple. For the conductivity measurements in wet air, the compressed air was humidified by passing through boiling water at a flow rate of 100 mL min⁻¹ and then flowed into the jig sealed in a vertical furnace to be heated from 20 to 600 °C. The temperature of wet air around the pellet was read by a thermocouple linked to Solartron 1470E CellTest System.

To rule out the effect of water or solutions surrounding pellets on the ionic conductivity, the conductivity of pellets was also measured using a home-made fuel cell jig shown in Supplementary Fig. 33. The electrolyte pellet was coated with 1 cm² of silver paste on two sides, matching the active area of the fuel cell testing jig. Water or KOH (85%, Thermo Scientific) solutions were pumped passing through the two chambers of jig. The electrolyte pellet was sealed by silicone gaskets to avoid being covered and crossed by solutions.

Before the conductivity measurements, all the pellets were heated in hot water at 90 °C for 20 h and washed to get rid of second phase SrY₂O₄ and the hydrated products. This process was repeated three times for each sample.

Electronic conductivity of the pellet was measured by a pseudo four-terminal DC method on a Solartron 1470E CellTest System. To work out the resistance caused by electronic conduction, 1 V constant DC voltage was applied on the pellet⁴¹. After the current had been saturated, the direct current electrical resistance (R_{DC}) was calculated from applied voltage (V) and saturated current (I_{sat})^{37,78}. Then the electrical conductivity (σ_e) was calculated on the basis of thickness, λ , and effective cross-sectional area of the electrolyte pellet, A , as follows^{37,41}:

$$R_{DC} = V/I_{sat}, \quad (4)$$

$$\sigma_e = \lambda/(R_{DC} \times A). \quad (5)$$

Electrochemical impedance spectrum (EIS) was acquired using a Solartron 1455 frequency response analyser (FRA) with 10 mV amplitude and frequency range of 1 MHz to 0.01 Hz to measure total conductivities (σ_t). Based on the relation between electronic conductivity and total conductivity, the ionic conductivity σ_i is calculated as:

$$\sigma_i = \sigma_t - \sigma_e \quad (6)$$

The electronic conduction transfer number (t_e) is $\sigma_e/\sigma_t \times 100\%$. Then the corresponding ion transfer number (t_i) can be measured as follows:

$$t_i = (1 - \sigma_e/\sigma_t) \times 100\% \quad (7)$$

The activation energy (E_a) for ion transport was calculated by the following equation:

$$\ln(\sigma T) = \ln \sigma_0 - \frac{E_a}{RT} \quad (8)$$

where σ_0 is a preexponential factor, R is the gas constant, and T is temperature.

EIS tested in a range from the high frequency of 10 MHz were performed using VIONIC potentiostat from Metrohm Autolab, controlled by Intello 1.4.0 software. The equivalent circuit fit, simulations, and Kramers–Kronig test were performed by using Nova 2.1.6 software.

The conductivity and pH of the water used to soak the pellets and measurement jig during the test have been recorded immediately after the completion of the conductivity measurement for pellets in water. Conductivity and temperature of water were measured with an Orion Star™ A212 Conductivity Benchtop Metre and an Orion 013005MD 4-Cell Conductivity Probe (Thermo Scientific). The pH value of water was measured with an Orion Star™ A214 PH/ISE Benchtop Meter (Thermo Scientific) and a glass bulb pH electrode (ELIT PH-2011). The results are summarized in Supplementary Table 4.

Identification of the charge carrier in ionic conductors

In order to determine which ion was conducted by the solid ionic conductors, a concentration cell with Ag/Ag₂O electrodes was made according to the method described in a previous report³⁷. A perovskite oxide pellet was clamped between two chambers of the H-cell filled with NaOH solution (Supplementary Fig. 10). A Nafion™ 212 membrane (FuelCellStore) and an anion exchange membrane (AEM) (Fumapem FAA, FuelCellStore) purchased commercially were measured for comparison (details in Supplementary Note 1).

In order to further verify that the cation transport number measured in the concentration cell represents proton conduction, the proton transference number (t_+) of SZYO20 pellet at room temperature was determined by chronoamperometry in conjunction with EIS measurements^{41,79}. The corresponding measurements were similar to the conductivity measurements of electrolyte pellet in water using the jig shown in Supplementary Fig. 33. Nafion membranes were used as blocking electrodes to fabricate Nafion|SZYO20|Nafion assembly (Supplementary Fig. 11a) to block all the ions except protons at the electrolyte/electrode interface^{78,80,81}. The initial current (I_0) and final steady-state current (I_s) were recorded when a DC polarisation voltage (V) of 1 V was applied across the cell. A.c. impedance measurements were carried out to determine the electrolyte resistances before (R_0) and after (R_s) the polarisation process. t_+ was calculated as follows:

$$t_+ = \frac{I_s(V - I_0 R_0)}{I_0(V - I_s R_s)} \quad (9)$$

KIE measurements

The SZYO2O electrolyte pellet was firstly treated in deionized water at 90 °C for 20 h (repeated three times), and then dried in a vacuum oven at 120 °C overnight to remove the adsorbed water as much as possible. The conductivity was then measured after the pre-treated pellet was stored in deuterium water (D₂O) overnight. The kinetic isotope effect (KIE) is the ratio of ion conductivity of pellets in H₂O to that in D₂O⁴¹.

Density functional theory simulations

All density functional theory (DFT) simulations were performed with the CP2K code, which uses a mixed Gaussian/plane-wave basis set⁸². Double polarisation quality Gaussian basis sets⁸³ and plane-wave cutoff of 400 Ry for the auxiliary grid were used in conjunction with the Goedecker-Teter-Hutter pseudopotentials⁸⁴. The DFT calculations including geometry relaxation, single point energies, and ab initio molecular dynamics (AIMD) simulations were conducted using the Perdew-Burke-Ernzerhof (PBE) exchange-correlation functional⁸⁵, with Grimme's D3 van der Waals correction (PBE + D3)⁸⁶. All DFT calculations were performed in the Γ -point approximation with a sufficiently large supercell. AIMD simulations within the Born-Oppenheimer approximation were performed in the canonical (NVT) ensemble. A timestep of 0.5 fs was used for the integration of the equation of motion, and the simulations were run for 20 ps (40,000 AIMD steps following 2,000 steps of equilibration run that has a strong thermostat coupling). The temperature of the AIMD simulation was 400 K, which was controlled by the canonical sampling through velocity rescaling thermostat⁸⁷ using a time constant of 50 fs.

Electrode preparation for fuel cell measurement

Plain carbon fibre cloth (0.35 mm thickness, E-TEK) was used as the substrate for the catalysts. The carbon cloth electrode (1 × 1 cm²) was sonicated in diluted hydrochloric acid, deionized water, and isopropanol for 1 min respectively. PtIr/C catalysts (20 wt% of metals loading) were prepared by the borohydride reduction process⁸⁸ using K₂PtCl₆ (Pt 39.6%, Thermo Scientific™), IrCl₃·3H₂O (53–56% Ir, Thermo Scientific™) and Vulcan XC72 carbon black (Cabot) as precursors. The atomic ratio of Pt:Ir is 50:50. The catalyst ink was made up of 80 mg PtIr/C powder, 500 μ L isopropanol and 145 μ L 5 wt% Nafion solution (Sigma Aldrich). The ink slurry was ultrasonicated for 1 h and then brushed onto the pre-treated carbon cloth. The electrode was dried in an oven at 80 °C. The loading of PtIr was about 1.2 mg cm². The Pt/C electrode (20 wt% Pt on carbon black, Alfa Aesar) was prepared in the same way and the loading of Pt was about 1.3 mg cm².

Hydrogen fuel cell fabrication and measurements

A SZYO2O pellet (1.8 mm of thickness, 19.2 mm of diameter) was employed as the electrolyte. The symmetric hydrogen fuel cell was assembled using Pt/C electrode as both the anode and cathode. The loading of Pt is about 1.3 mg cm². The effective area of the fuel cell was 1 × 1 cm². Hydrogen gas was passing through a humidifier to flow into the anode at 5 mL min⁻¹, whilst 20 mL min⁻¹ humidified compressed air was flowing into the cathode field of fuel cell system. The pressure of both hydrogen and compressed air is at ambient pressure. The polarisation curves and power density curves were measured through a Solartron 1287A electrochemical interface controlled by electrochemical software CorrWare/CorrView. The EIS data of the fuel cell was collected by the Solartron 1260 A Electrochemical Station at a frequency range of 1 MHz to 0.01 Hz and fixed potential of 10 mV bias.

Direct ammonia fuel cell fabrication and measurements

A SZYO2O pellet (1.3 mm of thickness, 19.2 mm of diameter) was used as the electrolyte. PtIr/C and Pt/C electrode was used as ammonia oxidation reaction (AOR) anode and oxygen reduction reaction

(ORR) cathode respectively in direct ammonia fuel cell (DAFC) measurements. The loading of PtIr was about 1.2 mg cm² and the loading of Pt was about 1.3 mg cm². The effective area of the fuel cell was 1 × 1 cm². An ammonia solution, i.e., 35 wt% NH₃H₂O (35%, Fisher Chemical™) or 35 wt% NH₃H₂O + 3 M KOH, was pumped at a flow rate of 1 mL min⁻¹ into anode channels. Compressed air was passing through 100 °C humidifier at 20 mL min⁻¹ then into the cathodic chamber. The durability test of the DAFC was carried out at a fixed current density of 4 mA cm² at an operating temperature of 60 °C a few days after the polarisation curves test. The cell temperature was controlled by heating cartridges sensed by thermocouples. The pressure of both the ammonia solution at the anode and compressed air at the cathode is at ambient pressure. The fuel cell performance was measured by a Solartron 1287 A Electrochemical Interface coupled with a Solartron 1260 controlled by electrochemical software CorrWare/CorrView and Z-Plot/Z-view. The a.c. impedance was measured in the frequency range between 1 MHz and 0.01 Hz at the amplitude of the a.c. signal 10 mV. The polarisation curves were obtained at different temperatures of the fuel cell and a scan rate of 5 mV s⁻¹ was used in the measurements. The commercial AEM (Fumapem FAA-3–50, FuelCellStore) with 50 μ m thickness was also employed in fuel cell measurements for comparison.

Electrolysis of H₂¹⁸O and D₂O using dense CZYO2O as the electrolyte

H₂¹⁸O and D₂O were bought from CK Isotopes Limited and Sigma-Aldrich respectively. A CZYO2O pellet sintered at 1500 °C (0.8 mm of thickness, 16.7 mm of diameter) was used as the electrolyte. RuO₂ (Sigma Aldrich) and Pt/C was used as oxygen evolution reaction (OER) anode and hydrogen evolution reaction (HER) cathode catalysts respectively in the electrolytic cell, and the electrode preparation method is the same as that of fuel cells. The effective area of the cell was 1 × 1 cm². A total of 20% H₂¹⁸O, pure D₂O or the solution of 1 M KOH dissolved in D₂O was pumped at a flow rate of 1 mL min⁻¹ into cathode channels while pure H₂¹⁶O water was pumped into the anodic chamber. The electrolysis performance was measured by the same set-up as DAFC. The durability test of the electrolysis cell was carried out at a fixed cell voltage of 2 V. The polarisation curves were obtained at a scan rate of 5 mV s⁻¹.

Data availability

The data that support the findings of this study are available from the corresponding author upon reasonable request. Source data are provided with this paper. Figshare <https://doi.org/10.6084/m9.figshare.24718497> Source data are provided with this paper.

References

1. Steele, B. C. H. & Heinzel, A. Materials for fuel-cell technologies. *Nature* **414**, 345–352 (2001).
2. Tao, S. & Irvine, J. T. S. A redox-stable efficient anode for solid-oxide fuel cells. *Nat. Mater.* **2**, 320–323 (2003).
3. Zhang, L. et al. A review of the chemical compatibility between oxide electrodes and electrolytes in solid oxide fuel cells. *J. Power Sources* **492**, 229630 (2021).
4. Takahashi, T. & Iwahara, H. Solid-state ionics - protonic conduction in perovskite type oxide solid-solutions. *Rev. De. Chim. Miner.* **17**, 243–253 (1980).
5. Ishihara, T., Matsuda, H. & Takita, Y. Doped LaGaO₃ perovskite-type oxide as a new oxide ionic conductor. *J. Am. Chem. Soc.* **116**, 3801–3803 (1994).
6. Minh, N. Q. in *Solid Oxide Fuel Cells:(SOFC VI): Proceedings of the Sixth International Symposium*. 127 (The Electrochemical Society).
7. Nernst, W. On the electrolytic conduction of solid bodies at high temperatures. *Z. Electrochem* **6**, 41–43 (1899).

8. Iwahara, H., Yajima, T., Hibino, T., Ozaki, K. & Suzuki, H. Protonic conduction in calcium, strontium and barium zirconates. *Solid State Ion.* **61**, 65–69 (1993).
9. Tao, S. & Irvine, J. T. S. A stable, easily sintered proton-conducting oxide electrolyte for moderate-temperature fuel cells and electrolyzers. *Adv. Mater.* **18**, 1581–1584 (2006).
10. Irvine, J. et al. Roadmap on inorganic perovskites for energy applications. *J. Phys.: Energy* **3**, 031502 (2021).
11. Norby, T. Solid-state protonic conductors: principles, properties, progress and prospects. *Solid State Ion.* **125**, 1–11 (1999).
12. Yang, L. et al. Enhanced sulfur and coking tolerance of a mixed ion conductor for SOFCs: BaZr_{0.1}Ce_{0.7}Y_{0.2}-xYb_xO_{3-δ}. *Science* **326**, 126–129 (2009).
13. Feng, M. & Goodenough, J. B. Improved oxide ion electrolytes. *MRS Online Proceedings Library (OPL)* **369**, 333–342 (1994).
14. Regalado Vera, C. Y. et al. A mini-review on proton conduction of BaZrO₃-based perovskite electrolytes. *J. Phys.: Energy* **3**, 032019 (2021).
15. Kreuer, K.-D. Proton-conducting oxides. *Annu. Rev. Mater. Res.* **33**, 333–359 (2003).
16. Choi, S. et al. Exceptional power density and stability at intermediate temperatures in protonic ceramic fuel cells. *Nat. Energy* **3**, 202–210 (2018).
17. Wang, J. et al. Poly (aryl piperidinium) membranes and ionomers for hydroxide exchange membrane fuel cells. *Nat. Energy* **4**, 392–398 (2019).
18. Kim, S., Anselmi-Tambtirini, U., Park, H. J., Martin, M. & Munir, Z. A. Unprecedented room-temperature electrical power generation using nanoscale fluorite-structured oxide electrolytes. *Adv. Mater.* **20**, 556–559 (2008).
19. Kreuer, K. D. Proton conductivity: materials and applications. *Chem. Mater.* **8**, 610–641 (1996).
20. Papac, M., Stevanović, V., Zakutayev, A. & O’Hayre, R. Triple ionic-electronic conducting oxides for next-generation electrochemical devices. *Nat. Mater.* **20**, 301–313 (2021).
21. Yang, X. et al. Mechanism of proton conduction in doped barium cerates: a first-principles study. *J. Phys. Chem. C.* **124**, 8024–8033 (2020).
22. Yajima, T., Suzuki, H., Yogo, T. & Iwahara, H. Protonic conduction in SrZrO₃-based oxides. *Solid State Ion.* **51**, 101–107 (1992).
23. Bonanos, N., Ellis, B. & Mahmood, M. Oxide ion conduction in ytterbium-doped strontium cerate. *Solid State Ion.* **28**, 579–584 (1988).
24. Buannic, L., Blanc, F., Middlemiss, D. S. & Grey, C. P. Probing cation and vacancy ordering in the dry and hydrated yttrium-substituted BaSnO₃ perovskite by NMR spectroscopy and first principles calculations: implications for proton mobility. *J. Am. Chem. Soc.* **134**, 14483–14498 (2012).
25. Wu, J., Li, L. P., Espinosa, W. T. P. & Haile, S. M. Defect chemistry and transport properties of Ba_xCe_{0.85}Mo_{0.15}O_{3-δ}. *J. Mater. Res.* **19**, 2366–2376 (2004).
26. Bjørheim, T. S., Hoedl, M. F., Merkle, R., Kotomin, E. A. & Maier, J. Proton, hydroxide ion, and oxide ion affinities of closed-shell oxides: importance for the hydration reaction and correlation to electronic structure. *J. Phys. Chem. C.* **124**, 1277–1284 (2019).
27. Zhong, P. et al. Protonic Conduction in La₂NiO_{4+δ} and La_{2-x}Ax-NiO_{4+δ} (A= Ca, Sr, Ba) Ruddlesden–Popper Type Oxides. *Adv. Energy Mater.* **12**, 2200392 (2022).
28. Tao, S. & Irvine, J. T. A stable, easily sintered proton-conducting oxide electrolyte for moderate-temperature fuel cells and electrolyzers. *Adv. Mater.* **18**, 1581–1584 (2006).
29. Azizi, M., Paydar, M. & Alafzadeh, M. Influence of the calcination temperature and fuel composition on synthesis of BaZr_{0.8}Y_{0.2}O_{3-δ} by solution combustion method for high proton conductivity. *Int. J. Adv. Sci. Technol.* **96**, 11–20 (2016).
30. Tanaka, H., Uchiyama, K., Shimizu, T. & Funakubo, H. Optimization of deposition conditions of yttrium doped-SrZrO₃ thin films fabricated by pulsed laser deposition. *J. Ceram. Soc. Jpn.* **128**, 436–440 (2020).
31. HUNG, I.-M. et al. Material characterization and electrochemical performance of Sr(Ce_{0.6}Zr_{0.4})_{0.8}Y_{0.2}O_{3-δ} proton conducting ceramics prepared by EDTA-citrate complexing and solid-state reaction methods. *J. Ceram. Soc. Jpn.* **123**, 187–192 (2015).
32. Otsuka-Yao-Matsuo, S., Omata, T., Ueno, S. & Kita, M. Photo-bleaching of methylene blue aqueous solution sensitized by composite powders of titanium oxide with SrTiO₃, BaTiO₃, and CaTiO₃. *Mater. Trans.* **44**, 2124–2129 (2003).
33. Opravil, T., Ptacek, P., Soukal, F., Bartonickova, E. & Wasserbauer, J. Solid-state synthesis of SrY₂O₄ and SrSm₂O₄. *J. Therm. Anal. Calorim.* **123**, 181–194 (2016).
34. Slodczyk, A. et al. Phase transitions in the H⁺-conducting perovskite ceramics by the quasi-elastic neutron and high-pressure Raman scattering. *Ionics* **14**, 215–222 (2008).
35. Lu, Y., Zhao, C.-Z., Huang, J.-Q. & Zhang, Q. The timescale identification decoupling complicated kinetic processes in lithium batteries. *Joule* **6**, 1172–1198 (2022).
36. Soni, R. et al. Lithium-sulfur battery diagnostics through distribution of relaxation times analysis. *Energy Storage Mater.* **51**, 97–107 (2022).
37. Takeguchi, T. et al. Layered Perovskite Oxide: A Reversible Air Electrode for Oxygen Evolution/Reduction in Rechargeable Metal-Air Batteries. *J. Am. Chem. Soc.* **135**, 11125–11130 (2013).
38. Kim, J. et al. Triple-conducting layered perovskites as cathode materials for proton-conducting solid oxide fuel cells. *ChemSusChem* **7**, 2811–2815 (2014).
39. Bonanos, N., Ellis, B., Knight, K. & Mahmood, M. Ionic conductivity of gadolinium-doped barium cerate perovskites. *Solid State Ion.* **35**, 179–188 (1989).
40. Pergolesi, D. et al. High proton conduction in grain-boundary-free yttrium-doped barium zirconate films grown by pulsed laser deposition. *Nat. Mater.* **9**, 846–852 (2010).
41. Qian, X. T. et al. CdPS₃ nanosheets-based membrane with high proton conductivity enabled by Cd vacancies. *Science* **370**, 596–600 (2020).
42. Gottesfeld, S. et al. Anion exchange membrane fuel cells: Current status and remaining challenges. *J. Power Sources* **375**, 170–184 (2018).
43. Buannic, L., Blanc, F., Hung, I., Gan, Z. & Grey, C. P. Probing the local structures and protonic conduction pathways in scandium substituted BaZrO₃ by multinuclear solid-state NMR spectroscopy. *J. Mater. Chem.* **20**, 6322–6332 (2010).
44. Buannic, L., Sperrin, L., Dervişoğlu, R., Blanc, F. & Grey, C. P. Proton distribution in Sc-doped BaZrO₃: a solid state NMR and first principle calculations analysis. *Phys. Chem. Chem. Phys.* **20**, 4317–4328 (2018).
45. Miyoshi, S. et al. Low-temperature protonic conduction based on surface protonics: an example of nanostructured yttria-doped zirconia. *Chem. Mater.* **26**, 5194–5200 (2014).
46. Jaegers, N. R., Wang, Y. & Hu, J. Z. Thermal perturbation of NMR properties in small polar and non-polar molecules. *Sci. Rep.* **10**, 1–9 (2020).
47. Kawata, K., Maekawa, H., Nemoto, T. & Yamamura, T. Local structure analysis of YSZ by Y-89 MAS-NMR. *Solid State Ion.* **177**, 1687–1690 (2006).
48. Bielecki, J., Parker, S. F., Mazzei, L., Börjesson, L. & Karlsson, M. Structure and dehydration mechanism of the proton conducting oxide Ba₂In₂O₅(H₂O)_x. *J. Mater. Chem. A* **4**, 1224–1232 (2016).
49. Bhuvanesh, N. et al. Topotactic H⁺/Li⁺ ion exchange on La_{2/3-x}Li_{3x}TiO₃: New metastable perovskite phases La_{2/3-x}TiO_{3-3x}

- (OH) 3x and La_{2/3}-xTiO₃-3x/2 obtained by further dehydration. *Mater. Res. Bull.* **33**, 1681–1691 (1998).
50. Slodczyk, A., Colomban, P., Willemijn, S., Lacroix, O. & Sala, B. Indirect Raman identification of the proton insertion in the high-temperature [Ba/Sr][Zr/Ti] O₃-modified perovskite protonic conductors. *J. Raman Spectrosc.* **40**, 513–521 (2009).
51. Colomban, P., Tran, C., Zaafrani, O. & Slodczyk, A. Aqua oxyhydroxycarbonate second phases at the surface of Ba/Sr-based proton conducting perovskites: a source of confusion in the understanding of proton conduction. *J. Raman Spectrosc.* **44**, 312–320 (2013).
52. Chen, Q. et al. Effect of compressive strain on the Raman modes of the dry and hydrated BaCeO₃·8H₂O proton conductor. *J. Phys. Chem. C* **115**, 24021–24027 (2011).
53. Sears, V. F. Neutron scattering lengths and cross sections. *Neutron N.* **3**, 26–37 (1992).
54. Lee, J. G. et al. Use of interplay between a-site non-stoichiometry and hydroxide doping to deliver novel proton-conducting perovskite oxides. *Adv. Energy Mater.* **11**, 2101337 (2021).
55. Ahmed, I. et al. Location of deuteron sites in the proton conducting perovskite BaZrO₃·50nD₂O. *J. Alloy. Compd.* **450**, 103–110 (2008).
56. Kinyanjui, F. G. et al. Crystal structure and proton conductivity of BaSn_{0.6}Sc_{0.4}O_{3-δ}: insights from neutron powder diffraction and solid-state NMR spectroscopy. *J. Mater. Chem. A* **4**, 5088–5101 (2016).
57. Islam, M. S. Computer modelling of defects and transport in perovskite oxides. *Solid State Ion.* **154**, 75–85 (2002).
58. Jeerh, G., Zou, P., Zhang, M. & Tao, S. W. Perovskite oxide LaCr_{0.25}Fe_{0.25}Co_{0.5}O_{3-δ} as an efficient non-noble cathode for direct ammonia fuel cells. *Appl. Catal. B: Environ.* **319**, 121919 (2022).
59. Zhang, M. et al. Recent development of perovskite oxide-based electrocatalysts and their applications in low to intermediate temperature electrochemical devices. *Mater. Today* **49**, 351–377 (2021).
60. Jeerh, G., Zhang, M. & Tao, S. W. Recent progress on ammonia fuel cells and their potential applications. *J. Mater. Chem. A* **9**, 727–752 (2021).
61. Lan, R. & Tao, S. Direct ammonia alkaline anion-exchange membrane fuel cells. *Electrochem. Solid State Lett.* **13**, B83–B86 (2010).
62. Zhao, Y. et al. An efficient direct ammonia fuel cell for affordable carbon-neutral transportation. *Joule* **3**, 2472–2484 (2019).
63. Li, Y. et al. High-performance ammonia oxidation catalysts for anion-exchange membrane direct ammonia fuel cells. *Energy Environ. Sci.* **14**, 1449–1460 (2021).
64. Lan, R., Irvine, J. T. S. & Tao, S. W. Ammonia and related chemicals as potential indirect hydrogen storage materials. *Int. J. Hydrog. Energy* **37**, 1482–1494 (2012).
65. Rathoure, A. K. & Pramanik, H. Electrooxidation study of methanol using H₂O₂ and air as mixed oxidant at cathode in air breathing microfluidic fuel cell. *Int. J. Hydrog. Energy* **41**, 15287–15294 (2016).
66. Sun, X., Gu, J., Han, D. & Norby, T. Quantifiable models for surface protonic conductivity in porous oxides—case of monoclinic ZrO₂. *Phys. Chem. Chem. Phys.* **24**, 11856–11871 (2022).
67. Sun, X. et al. Surface protonic conductivity in chemisorbed water in porous nanoscopic CeO₂. *Appl. Surf. Sci.* **611**, 155590 (2023).
68. Draksharapu, A. *Shedding Light on Active Species in Fe, Ni and Cu Catalysis: Photochemical, Spectroscopic and Electrochemical Studies*. PhD thesis, Univ. Groningen (2013).
69. Litvak, I., Anker, Y. & Cohen, H. On-line in situ determination of deuterium content in water via FTIR spectroscopy. *RSC Adv.* **8**, 28472–28479 (2018).
70. Velez, A. A. I. et al. Properties of the PVA-VAVD KOH blend as a gel polymer electrolyte for zinc batteries. *Gels* **7**, 256 (2021).
71. Pan, Y. et al. Direct evidence of boosted oxygen evolution over perovskite by enhanced lattice oxygen participation. *Nat. Commun.* **11**, 2002 (2020).
72. Dai, J. et al. Hydrogen spillover in complex oxide multifunctional sites improves acidic hydrogen evolution electrocatalysis. *Nat. Commun.* **13**, 1189 (2022).
73. Huang, P.-n & Petric, A. Electrical conduction of yttrium-doped strontium zirconate. *J. Mater. Chem.* **5**, 53–56 (1995).
74. Shao, L., Si, F., Fu, X.-Z. & Luo, J.-L. Stable SrCo_{0.7}Fe_{0.2}Zr_{0.1}O_{3-δ} cathode material for proton conducting solid oxide fuel cell reactors. *Int. J. Hydrog. Energy* **43**, 7511–7514 (2018).
75. Toby, B. H. & Von Dreele, R. B. GSAS-II: the genesis of a modern open-source all purpose crystallography software package. *J. Appl. Crystallogr.* **46**, 544–549 (2013).
76. Ibberson, R. M. Design and performance of the new supermirror guide on HRPD at ISIS. *Nucl. Instrum. Methods Phys. Res. Sect. A: Accelerators, Spectrometers, Detect. Associated Equip.* **600**, 47–49 (2009).
77. Arnold, O. et al. Mantid—Data analysis and visualization package for neutron scattering and μ SR experiments. *Nucl. Instrum. Methods Phys. Res. Sect. a: accelerators, spectrometers, Detect. associated Equip.* **764**, 156–166 (2014).
78. Wang, S., Yan, M., Li, Y., Vinado, C. & Yang, J. Separating electronic and ionic conductivity in mix-conducting layered lithium transition-metal oxides. *J. Power Sources* **393**, 75–82 (2018).
79. Evans, J., Vincent, C. A. & Bruce, P. G. Electrochemical measurement of transference numbers in polymer electrolytes. *Polymer* **28**, 2324–2328 (1987).
80. Gilbert, T. A. *Measuring Proton Transport Through Two-Dimensional Materials*. MSc thesis, Vanderbilt Univ. (2020).
81. Huggins, R. A. Simple method to determine electronic and ionic components of the conductivity in mixed conductors a review. *Ionics* **8**, 300–313 (2002).
82. Kühne, T. D. et al. CP2K: an electronic structure and molecular dynamics software package—Quickstep: Efficient and accurate electronic structure calculations. *J. Chem. Phys.* **152**, 194103 (2020).
83. VandeVondele, J. & Hutter, J. Gaussian basis sets for accurate calculations on molecular systems in gas and condensed phases. *J. Chem. Phys.* **127**, 114105 (2007).
84. Goedecker, S., Teter, M. & Hutter, J. Separable dual-space Gaussian pseudopotentials. *Phys. Rev. B* **54**, 1703 (1996).
85. Perdew, J. P., Burke, K. & Ernzerhof, M. Generalized gradient approximation made simple. *Phys. Rev. Lett.* **77**, 3865 (1996).
86. Grimme, S., Antony, J., Ehrlich, S. & Krieg, H. A consistent and accurate ab initio parametrization of density functional dispersion correction (DFT-D) for the 94 elements H–Pu. *J. Chem. Phys.* **132**, 154104 (2010).
87. Bussi, G., Donadio, D. & Parrinello, M. Canonical sampling through velocity rescaling. *J. Chem. Phys.* **126**, 014101 (2007).
88. Assumpção, M. H. et al. Direct ammonia fuel cell performance using Pt/C as anode electrocatalysts. *Int. J. Hydrog. Energy* **39**, 5148–5152 (2014).

Acknowledgements

The authors thank EPSRC (Grant No. EP/W035529/1) and Innovate UK (Grant Nos. 104010 and 133714) for funding. One of the authors (P.Z.) thanks the China Scholarship Council for PhD studentship (No. 201908430195). The authors thank the X-ray Diffraction Research Technology Platform for access to the XRD measurement equipment and the UK High-field solid-state NMR facility for access to the solid state NMR at the University of Warwick. The authors thank the use of the Sulis supercomputer through the HPC Midlands+ Consortium, and the

ARCHER2 supercomputer through membership of the U.K.'s HPC Materials Chemistry Consortium, which are funded by EPSRC Grant Nos. EP/T022108/1 and EP/R029431/1, respectively. The authors thank Dr. James Town for performing STA measurements. The authors thank Dr. Ben Breeze for performing Raman measurements on H₂¹⁸O samples and setting up high high-temperature Raman measurement stage.

Author contributions

S.T. conceived and supervised the project. S.T., P.Z. designed the experiments. P.Z. performed the experiments except for solid-state NMR, neutron diffraction, STEM measurement, and DFT simulation, D.I. performed the experiments and data analysis of solid-state NMR. S.L. performed DFT simulations and related data analysis. A.J.B. analysed the neutron diffraction data. S.C. helped with SEM/EDX experiments, M.Z. helped with drawing and plotting. Y.H. helped with TEM measurements and analysis. A.D.F. and C.M.H. collected the HRPD neutron diffraction data. S.T. and A.J.B. carried out Rietveld refinement. S.T. and P.Z. analysed the data and wrote the manuscript with input from D.I. for the solid-state NMR part, input from S.L. for DFT part, and input from A.J.B. for the neutron diffraction part. All authors commented on the manuscript.

Competing interests

S.T. and P.Z. are listed as co-inventors on a pending UK & National patent application related to this work filed by University of Warwick. All other authors declare no competing interests.

Additional information

Supplementary information The online version contains supplementary material available at <https://doi.org/10.1038/s41467-024-45060-1>.

Correspondence and requests for materials should be addressed to Shanwen Tao.

Peer review information *Nature Communications* thanks the anonymous, reviewers for their contribution to the peer review of this work. A peer review file is available.

Reprints and permissions information is available at <http://www.nature.com/reprints>

Publisher's note Springer Nature remains neutral with regard to jurisdictional claims in published maps and institutional affiliations.

Open Access This article is licensed under a Creative Commons Attribution 4.0 International License, which permits use, sharing, adaptation, distribution and reproduction in any medium or format, as long as you give appropriate credit to the original author(s) and the source, provide a link to the Creative Commons licence, and indicate if changes were made. The images or other third party material in this article are included in the article's Creative Commons licence, unless indicated otherwise in a credit line to the material. If material is not included in the article's Creative Commons licence and your intended use is not permitted by statutory regulation or exceeds the permitted use, you will need to obtain permission directly from the copyright holder. To view a copy of this licence, visit <http://creativecommons.org/licenses/by/4.0/>.

© The Author(s) 2024